

MIT Open Access Articles

*RNA G-quadruplexes are globally unfolded
in eukaryotic cells and depleted in bacteria*

The MIT Faculty has made this article openly available. **Please share**
how this access benefits you. Your story matters.

Citation: Guo, Junjie U., and David P. Bartel. "RNA G-Quadruplexes Are Globally Unfolded in Eukaryotic Cells and Depleted in Bacteria." *Science* 353, no. 6306 (September 22, 2016): aaf5371–aaf5371.

As Published: <http://dx.doi.org/10.1126/science.aaf5371>

Publisher: American Association for the Advancement of Science (AAAS)

Persistent URL: <http://hdl.handle.net/1721.1/107226>

Version: Original manuscript: author's manuscript prior to formal peer review

Terms of Use: Article is made available in accordance with the publisher's policy and may be subject to US copyright law. Please refer to the publisher's site for terms of use.



RNA G-quadruplexes are globally unfolded in eukaryotic cells and depleted in bacteria

Junjie U. Guo^{1,2} and David P. Bartel^{1,2,3}

¹Howard Hughes Medical Institute, Whitehead Institute for Biomedical Research, Cambridge, MA 02142, USA

²Department of Biology, Massachusetts Institute of Technology, Cambridge, MA 02139, USA

³Corresponding author. Email: dbartel@wi.mit.edu

Short title: Transcriptome-wide probing of RNA G-quadruplexes

ABSTRACT

In vitro, some RNAs can form stable four-stranded structures known as G-quadruplexes. Although RNA G-quadruplexes have been implicated in post-transcriptional gene regulation and diseases, direct evidence for their formation in cells has been lacking. Here, we identified thousands of mammalian RNA regions that can fold into G-quadruplexes in vitro, but in contrast to previous assumptions, these regions were overwhelmingly unfolded in cells. Model RNA G-quadruplexes that were unfolded in eukaryotic cells were folded when ectopically expressed in *Escherichia coli*; however, they impaired translation and growth, which helps explain why we detected few G-quadruplex-forming regions in bacterial transcriptomes. Our results suggest that eukaryotes have a robust machinery that globally unfolds RNA G-quadruplexes, whereas some bacteria have instead undergone evolutionary depletion of G-quadruplex-forming sequences.

MAIN TEXT

Many cellular RNAs contain regions that fold into stable structures required for function (1, 2). These structures can be studied using chemical probes that modify accessible or flexible nucleotides (3-5). For example, dimethyl sulfate (DMS) methylates A and C residues that are not protected by Watson–Crick pairing or other interactions, and because these modifications stall reverse transcriptase, primer-extension reactions can detect modification and thereby report on the folding state of these nucleotides. DMS also penetrates living cells and modifies RNAs within these cells, and with high-throughput sequencing of global primer-extension products, the intracellular folding of numerous RNAs can be simultaneously monitored in a procedure called DMS-seq (6, 7). Analogous high-throughput methods have also been developed using cell-permeable SHAPE (selective 2' -hydroxyl acylation analyzed by primer extension) reagents (8, 9). These methods reveal important differences between RNA structures formed *in vivo* and those formed *in vitro* (7, 9). However, these high-throughput methods are designed to detect Watson–Crick pairing, which leaves the folding states of noncanonical structures difficult to assess.

One such noncanonical structure is the RNA G-quadruplex (RG4), in which four strands of RNA interact, either intramolecularly or intermolecularly, through the formation of two or more layers of G-quartets, in which each of four G residues pairs to two neighboring G residues (Fig. 1A) (10, 11). Due to the extensive hydrogen-bonding and base-stacking interactions, RG4 structures can be very stable, with *in vitro* melting temperatures well exceeding physiological temperatures. This stability typically depends on the presence of K^+ , which is the optimal size to bind at the center of two stacked G-quartets and thereby counter the otherwise repulsive partial negative charges that converge at the quadruplex core (Fig. 1A).

Because of the high stability of RG4 structures in vitro and the high concentration of K^+ in cells (typically >100 mM, well above that required for quadruplex formation), regions that fold into RG4 structures in vitro are generally assumed to fold into these structures in cells. Indeed, RG4s are implicated in control of mRNA processing and translation, with recently proposed roles in human diseases, such as cancer (12) and neurodegeneration (13). Supporting the idea that RG4s are folded in cells, immunostaining with G4-specific antibodies yields a detectable, albeit weak, RNase-sensitive signal in the cytoplasm (14). However, these immunostaining results leave open the possibility of folding during the processes of fixing, permeabilizing or staining cells, and even if this signal represented quadruplex formation in cells, it could not speak to either the sequence identities or the overall fraction of RG4 regions that fold in vivo.

Many RNAs with quadruplex-forming capacity

To systematically search for structure-forming potential in mammalian cellular RNAs, we exploited the ability of stable structures to stall reverse transcription. Poly(A)-selected mRNAs from mouse embryonic stem cells (mESCs) were randomly fragmented, and 60–80-nt fragments were ligated to a common 3' adapter used for global primer extension. Complementary DNAs (cDNAs) resulting from reverse transcription that stalled after only 20–45 nt of extension were purified and sequenced to identify the RT stops (Fig. 1B), using a procedure resembling that developed for DMS-seq (7). As illustrated for the *Eef2* (*Eukaryotic elongation factor 2*) mRNA and the *Malat1* (*Metastasis-associated lung-adenocarcinoma transcript 1*) noncoding RNA, most of the strong RT stops (65%) were at G nucleotides (Fig. 1, C and D and fig. S1; $p < 10^{-15}$, χ^2 test). Analysis of the flanking sequences of these strong RT stops at G nucleotides showed that

the 30 nucleotides upstream of the RT stops were also enriched in G (and depleted in C), particularly at positions –1 and –2 (92 and 66% G, respectively; Fig. 1E). In contrast, no enrichment was detected downstream, except for weak G enrichment at position +1 (38% G; Fig. 1E).

The upstream G enrichment, together with recent studies of individual transcripts (15), suggested that formation of intramolecular RG4 structures caused these strong RT stops. To test this possibility, we examined whether these RT stops were sensitive to the identity of the monovalent counter ion, and found that substituting K^+ in the RT reaction with either Na^+ or Li^+ greatly diminished the RT stops at G residues (Fig. 2, A and B, and fig. S2A). Another diagnostic feature of RG4s is their sensitivity to modification of the N7 position of G (Fig. 1A). Methylating this position by using DMS (16) under denaturing conditions (95°C, 0 mM K^+) also substantially diminished the RT stops at G residues, despite the presence of K^+ during RT (Fig. 2, A and B, and fig. S2B). Most strong RT stops that were K^+ -dependent were also DMS-sensitive (Fig. 2C and table S1; $p < 10^{-15}$, χ^2 test), and vice versa. Moreover, 6,140 (90%) of the 6,812 RT stops that exhibited ≥ 2 fold decrease in Na^+/Li^+ reactions and ≥ 2 fold decrease after 95°C DMS treatment were at G nucleotides (fig. S2C and table S1). In contrast, the 2,120 DMS-sensitive but K^+ -independent RT stops did not exhibit strong nucleotide enrichment at position 0 (fig. S2C), as would be expected for RT stops caused by other types of stable structures. Analysis of the remaining 672 RT stops that were K^+ -dependent and DMS-sensitive but not at G nucleotides showed that their upstream sequences were also somewhat enriched in G (fig. S2D), suggesting that at least some of these RT stops also involved RG4 structures that caused RT to stall before reaching the 3' -terminal G nucleotides. Collectively, these results indicated that most G-rich regions that caused strong RT stops did so by forming RG4 structures in vitro.

The four strands of RG4 structures typically assume a parallel orientation (17) (Fig. 1A). The circular dichroism spectra of the 60-nt regions upstream of K⁺-dependent strong RT stops in *Eef2* and *Malat1*, as well as that of a canonical RG4 sequence G₃A₂G₃A₂G₃A₂G₃ (hereafter referred to as the G3A2 quadruplex), exhibited a K⁺-dependent increase at 263 nm, diagnostic of parallel RG4 structures (17) (fig. S3).

Features of mammalian RG4 regions

Of the many endogenous RNA sequences with predicted RG4-forming potential (18), only ~100 have been experimentally tested (11, 19). Therefore, the 6,140 RG4 regions in the mESC transcriptome, 4,034 of which were non-overlapping, considerably expanded the repertoire of endogenous RNA sequences with experimentally supported RG4-forming capacity. Nonetheless, cellular transcripts presumably contain additional regions with intrinsic RG4-forming potential not detected in our experiment. For example, our strategy would miss 1) structures with stabilities insufficient to block RT, 2) structures spanning more than ~60 nt, which would be too large to reside within the RNA fragments assayed for RT stops, or 3) regions within transcripts that were not expressed in mESCs at levels sufficient to be detected in our sequencing.

To benchmark our method using previously supported examples, nearly all of which are in human transcripts (19), we performed RT-stop profiling on mRNA from human cell lines. 12,009 and 12,035 RG4 regions (6,506 and 6,281 non-overlapping regions) were identified in the HEK293T and HeLa transcriptome, respectively, with 7,852 non-overlapping regions identified in at least one of the two cell lines, and 4,935 identified in both cell lines (table S2). Of the known RG4 regions within detected mRNAs, approximately half were detected as K⁺-dependent strong RT stops (fig. S4A and table S2).

Recently, a high-throughput method has been developed to identify genomic sequences that can fold into DNA G-quadruplexes in vitro (20). Because DNA and RNA of the same sequence often have distinct three-dimensional structures and some regions of DNA are either not expressed as RNA or are expressed as spliced transcripts that do not match the DNA, we expected that many DNA- or RNA-specific G4 regions would exist. Indeed, only 0.16% of the recently identified DNA G4 regions corresponded to RG4 regions found in HeLa and HEK293T cells, and of the non-overlapping HeLa/HEK293T RG4 regions that uniquely mapped to the human genome, only 19% mapped to identified DNA G4 regions (fig. S4B).

Compared to control regions with matched nucleotide composition, the identified RG4 regions were more likely to have the four G-triplets needed to match the canonical RG4 motif (fig. S3C), $G_{\geq 3}N_xG_{\geq 3}N_xG_{\geq 3}N_xG_{\geq 3}$, in which each N_x represents a linker of any sequence ranging from 1 to ~ 7 nt in length (18). However, 37% of these regions had fewer than four G-triplets within 60 nt upstream of the RT stop (fig. S4C) and thus would be missed by most G4-searching algorithms (18). The 6,140 RG4 regions from mESCs were found in 2,792 transcripts (table S1), which included both mRNAs and noncoding RNAs, such as *Malat1*, which was sufficiently abundant to be analyzed despite its lack of a poly(A) tail. As previously predicted (18), RG4 regions were enriched within untranslated regions (UTRs) relative to mRNA coding sequences (CDSs) (Fig. 2E; $p < 10^{-15}$, χ^2 test), as might be expected if some of these regions have regulatory functions. However, G nucleotides within the 60-nt regions upstream of RT stops were not more conserved than G nucleotides within flanking regions (fig. S5), suggesting that the RG4 structure-forming capacity of most RG4 regions was not evolutionarily conserved.

In sum, RT-stop profiling identified thousands of RG4 regions in the mammalian transcriptomes, thereby expanding the catalog of experimentally supported endogenous RG4

regions by >100 fold. As predicted computationally (18), regions that form RG4 structures in vitro are not an esoteric feature of dozens of mRNAs but rather ubiquitous within mammalian transcriptomes, bringing to the fore the question of their in vivo folding status.

Globally unfolded RG4 regions in mESCs

To identify RG4 regions that are folded in cells, we combined RT-stop profiling with elements of DMS-seq (7) to develop to a method that measures, transcriptome-wide, the in vivo folding states of endogenous sequences with RG4-forming potential (Fig. 3A). In this method, cells are first treated with DMS, which rapidly enters and randomly methylates accessible N7 positions of G residues (4). RNA isolated from these cells is then subjected to RT-stop profiling. Although DMS modifies the N7 position of G more efficiently than it modifies the N1 and N3 positions of A and C residues, respectively (21), modification at N7 does not prevent Watson–Crick pairing and thus does not cause an RT stop. Nonetheless, RT-stop profiling can distinguish between RG4 regions that are folded in cells from those that are not because those that are folded in vivo are protected from modification at positions participating in the RG4 structure, enabling them to later refold during RT to generate RT stops, whereas those that are unfolded in cells can be irreversibly modified at residues that would otherwise participate in quadruplex formation in vitro, resulting in RT read-through and correspondingly attenuated RT stops (Fig. 3A).

Reasoning that the RT-stop signals of different RG4 regions might have different sensitivities to DMS treatment, we first determined, for each RG4 region, the difference in RT-stop signal observed when mRNAs were modified in vitro either with or without K^+ . On average, the mESC RG4 regions refolded and DMS-treated in the presence of K^+ had RT stops that were 2.5-fold stronger than those observed when refolding and treating in the absence of K^+ (median

2.1 fold), and 1,342 regions had a difference of ≥ 2 fold (Fig. 3B and table S3). These in vitro results confirmed that DMS accessibility with readout from RT-stop profiling could indeed report on the folding states of many RG4 regions.

To probe the intracellular folding state of these regions, we treated mESCs with DMS and extracted poly(A)-selected RNAs for RT-stop profiling. As a positive control, results within the 5.8S rRNA were analyzed as a DMS-seq experiment (monitoring RT stops at A and C nucleotides), which showed that, as expected (7), DMS probing in vivo captured known Watson–Crick pairing within the 5.8S rRNA, as well as the intermolecular pairing between the 5.8S and 28S rRNAs (fig. S6A). Moreover, the RT-stop signals for RG4s were highly correlated between biological replicates (fig. S6B, Pearson's $r = 0.88$). Inspection of the RG4 regions in both *Eef2* mRNA and *Malat1* indicated that these RG4 regions were accessible to DMS modification in vivo, as revealed by greatly reduced RT-stop signals (Fig. 3C). The signals observed for the in vivo-modified sample resembled those observed when omitting K^+ from the in vitro folding and modification reaction, which indicated that these RG4 regions were unfolded in mESCs (Fig. 3C).

To infer the folding state, DMS-probing assays must be performed within their dynamic range; beyond this range, a transiently unfolded region might instead appear to be mostly unfolded, as most the molecules eventually become modified. The RT-stop signal at RG4 regions diminished in the unfolded reference (0 mM K^+) but did not reach baseline (Fig. 3B and C), which indicated that our in vitro treatment left a fraction of these molecules unmodified and thus showed that our in vitro modification was within its dynamic range. Moreover, DMS modification of A's and C's in vivo resembled that observed for our in vitro references (fig. S6C), which indicated that our in vivo probing was also within the dynamic range of the assay.

We next expanded the analysis to 1,141 regions that retained a strong RT-stop signal (10 fold above background) when treated with DMS in the presence of K^+ in vitro and had at least a 50% reduction in that signal when K^+ was excluded. For each of these regions, an in vivo folding score was calculated in which the RT-stop signal observed in vivo was expressed relative to the range of signal observed in vitro, assigning scores of 1 and 0 to the signals observed in vitro with and without K^+ , respectively. In vivo folding scores for the 1,141 RG4 regions centered near 0 (median = 0.06) (Fig. 3D and table S3), which indicated that in mESCs, the folding of most RG4 regions resembled the unfolded state observed in vitro without K^+ . RG4 regions in 5' UTRs, CDSs and 3' UTRs, as well as those in noncoding RNAs, were similarly unfolded (fig. S6D). Treating mESCs with pyridostatin (PDS), a G4-stabilizing reagent (14, 15), induced a detectable but modest increase in global RG4 folding (0.04 increase in median folding score) (Fig. 3E; $p < 10^{-8}$, paired t-test).

Although most RG4 regions are unfolded in mESCs, we cannot rule out the possibility that a few RG4 structures form in cells but could not be distinguished from experimental variability, or escaped our detection for other reasons, such as stable folding even in the absence of K^+ . An inability of DMS to penetrate the cell and modify the regions cannot be a source of false-negatives, as the decrease in the RG4-specific RT stops observed for RNA isolated from DMS-treated cells confirmed that DMS was indeed able to access and efficiently modify these regions in vivo. To confirm the unfolded state of RG4 regions with strong canonical motifs, we inserted the G3A2 quadruplex into an mRNA 3' UTR, ectopically expressed the mRNA in HEK293T cells, and performed DMS modification followed by gene-specific primer extension. Again, the RT-stop pattern observed after DMS modification in vivo strongly resembled that

observed after modifying in vitro without K^+ (Fig. 3F and fig. S6E), further supporting the conclusion that RG4 regions are mostly unfolded in mammalian cells.

Globally unfolded RG4 regions in yeast cells

To determine whether the globally unfolded state of RG4 regions extends beyond mammalian cells, we applied our methods to the budding yeast *Saccharomyces cerevisiae*. We identified 744 strong RT stops within RNA isolated from exponentially growing yeast (table S4A), 133 of which were K^+ -dependent stops at G nucleotides. Among them, 47 showed ≥ 2 -fold difference in RT-stop signal when comparing samples probed after folding with and without K^+ (Fig. 4A and table S4B). The folding scores of endogenous RG4 regions centered near 0 (median = -0.15) (Fig. 4, B and C), again indicating a globally unfolded state. As observed in HEK293 cells, the ectopically expressed G3A2 quadruplex was also highly accessible to DMS, as indicated by an RT stop matching that observed for RNA modified in vitro without K^+ (Fig. 4D). These results indicate that the globally unfolded state of RG4 regions is a broadly conserved feature of eukaryotic cells.

SHAPE probing of RG4 regions

In addition to the chemical probes that modify the bases, such as DMS, probes that modify ribose 2'-hydroxyl groups with efficiency depending on the local chemical environment, known as SHAPE reagents, can provide useful tools for studying RNA structures (3, 5). Among these reagents, 2-methylnicotinic acid imidazolid (NAI) has been used to probe Watson–Crick RNA structures in cells (9, 22). To test whether NAI can also distinguish the folding states of RG4 regions, we used it to treat the G3A2 quadruplex folded in vitro with or without K^+ and

quantified its reactivity at each nucleotide using gene-specific primer extension, substituting Na^+ for K^+ in the RT reaction, so that modifications within RG4 regions could be detected (Fig. 5A). Whereas the formation of Watson–Crick structure typically decreases SHAPE reactivity, formation of the G3A2 quadruplex in the presence of K^+ increased NAI reactivity (Fig. 5A). Furthermore, the enhanced reactivity occurred at the last G residue of each of the first three G tracts of the G3A2 quadruplex (Fig. 5A), consistent with a recent report describing in vitro NAI probing of two other G-quadruplexes (23). Perhaps the transition between a G-tract and a short loop in a parallel RG4 structure bends the RNA backbone to expose the 2' -hydroxyl of the last residue of the G tract (fig. S7A) (24). In vivo NAI treatment of the G3A2 quadruplex ectopically expressed in *S. cerevisiae* generated a modification pattern resembling that observed for this region folded in vitro without K^+ (Fig. 5A), supporting the conclusion that this quadruplex is unfolded in yeast cells. Analogous results were observed for another model RG4, which had single-nucleotide U loops linking the G tracts (the G3U quadruplex) (fig. S7B).

To probe endogenous RG4 regions, we treated mESC RNA with NAI either in vitro (refolded with or without K^+) or in vivo, and used RT-stop profiling with Na^+ to determine the modification patterns (Fig. 5B). As with the G3A2 quadruplex, when folding endogenous RG4 regions in the presence of K^+ in vitro, we observed preferential modification of the last G residue in G-tracts followed by short loops (Fig. 5C and fig. S7C). This pattern generated greater unevenness of modifications among G nucleotides within the RG4 region, which we quantified by calculating the Gini coefficient (7) for each of the 310 non-overlapping endogenous RG4 regions that had sufficient read coverage (≥ 100 RT-stop reads at G nucleotides in each sample). Among these, 49 had a ≥ 0.1 increase in Gini coefficient when comparing the modification observed in vitro after folding with K^+ compared to that observed after folding without K^+ (Fig.

5D). For these 49 regions, we calculated in vivo folding scores calibrated on the Gini-coefficient differences observed in vitro (table S5). As observed with the DMS probing, the distribution of in vivo folding scores centered near 0 (median = -0.02) (Fig. 5E), indicating that the in vivo NAI modification patterns of most RG4 regions resembled those of the unfolded state.

NAI probing complements DMS probing in three respects. First, NAI preferentially modifies specific residues of folded RG4s, whereas DMS modifies residues of unfolded RG4s. Second, NAI modification generates RT stops without requiring RG4 refolding, whereas DMS probing requires the refolding of RG4 structures in the presence of K^+ to generate an RT stop. Third, NAI probing might detect less stable RG4 structures that do not stall RT in vitro and thereby escape identification using RT-stop profiling. However, unlike DMS probing of RG4 regions, NAI probing does not focus the signal onto a single RT-stop nucleotide, and it requires specific RG4 configurations, such as G-tracts followed by short loops, which also reduced the number of quantifiable RG4 regions. Nevertheless, the results from these two complementary chemical-probing methods both indicated that, despite the high intracellular K^+ concentration, RG4 regions are overwhelmingly unfolded in eukaryotic cells.

Robust RG4 unfolding in eukaryotic cells

Our results in eukaryotic cells resembled those of recent high-throughput studies showing that Watson–Crick secondary structures that form in vitro are frequently unfolded in cells (7, 9), except the intracellular unfolding of RG4 regions was more pervasive. Whereas the previous studies identify many instances in which Watson–Crick structures do form in vivo, as expected from the known Watson–Crick pairing within ribosomal RNAs, tRNAs, pri-microRNAs, mRNAs, etc., we found no compelling evidence for the folding of an RG4 region in eukaryotic

cells, which implies that these cells have a very effective molecular machinery that specifically remodels RG4s and maintains them in their unfolded state.

This remodeling presumably involves ATP-dependent processes. ATP depletion in yeast causes a global increase in Watson–Crick structures, suggesting that ATP-dependent processes, in particular ATP-dependent RNA helicases, play a major role in the cellular remodeling of these structures (7). Among the characterized ATP-dependent RNA helicases, DEAH box-containing helicase 36 (DHX36) accounts for most RG4-unfolding activity in HeLa cell extracts (25). To test whether DHX36 contributes to the globally unfolded state of RG4 regions in vivo, we applied DMS probing to mouse embryonic fibroblasts (MEFs) in which DHX36 was inducibly deleted through Cre-mediated recombination (26). The global distribution of folding scores was largely unchanged after DHX36 deletion, and values for individual RG4 regions were highly correlated before and after DHX36 deletion (fig. S8A–C), indicating that DHX36 was dispensable for the global unfolding of endogenous RG4 regions. We also tested whether ATP depletion affected RG4 folding and found that the ectopically expressed G3A2 quadruplex remained largely unfolded (fig. S8D). Although redundant functions with other helicases and the inability to completely deplete ATP might explain the negative results of these experiments, our results show that the mechanism responsible for remodeling RG4s and maintaining their unfolded state is robust to either the deletion of a key helicase known to unfold RG4 structures or the substantial depletion of ATP.

Folding of RG4 structures in bacteria

We next applied our methods to bacterial transcriptomes. Compared to the mammalian transcriptome, the *E. coli* transcriptome was substantially depleted in regions with K⁺-dependent

strong RT stops (Fig. 6A and table S6). Only 35 K⁺-dependent strong RT stops were identified in *E. coli*, of which only 14 (40%) were at G nucleotides. Among these 14, none had differential DMS accessibility when comparing the results of in vitro modification with and without K⁺ (table S6). Similar depletion was observed within the transcriptomes of the other two bacteria we examined, *Pseudomonas putida* and *Synechococcus* sp WH8102 (Fig. 6A and table S6), even though their genomes are more G-rich than mammalian genomes. Only one region within the transcriptomes of these two species passed our cutoffs for calculating an in vivo folding score (a *P. putida* region with a folding score of 0.5, table S6).

Having acquired evidence for only a single, weak RG4 region in endogenously expressed bacterial RNA, we ectopically expressed the G3A2 quadruplex within the 3' UTR of an *mCherry* transcript and probed its folding state in *E. coli*. In contrast to our results in eukaryotic cells, the strong RT stop corresponding to the G3A2 quadruplex was resistant to in vivo DMS modification, indicating that this region was folded in *E. coli* cells (Fig. 6B and C). Likewise, the G3U quadruplex, was also folded in *E. coli* (Fig. 6C). Although intracellular NAI probing of the G3A2 quadruplex was inconclusive, intracellular NAI probing of the G3U quadruplex generated the modification pattern specific to that of the folded G3U quadruplex (fig. S9), confirming that RG4 folding rather than protein binding protected the region from DMS modification in vivo. Thus, RG4 regions are permitted to fold in *E. coli* but are strongly depleted among endogenous *E. coli* RNAs.

To understand this depletion, we compared the growth of strains that expressed G3A2 or G3U quadruplexes to those of strains that expressed the corresponding quadruplex mutants in which point substitutions abolished RG4-forming capacity and found that the RG4-expressing strains grew more slowly than the corresponding mutant-expressing strains (Fig. 6D). Moreover,

these growth defects were exacerbated after introducing stop-codon mutations that caused the *mCherry* coding sequence to extend through the RG4 regions (Fig. 6D). Although effects from the RG4 regions in UTRs might be attributable to either RNA or DNA quadruplex formation, the enhanced growth defects observed after introducing stop-codon mutations were attributable to only RG4 structures.

To determine the influence of folded RG4 structures on translation, we examined the translation products from each of the strains. Consistent with a previous study (27), RG4 regions downstream of the stop codon did not substantially influence mCherry production. In contrast, the G3A2 quadruplex upstream of the stop codon caused read-through of the stop codon and/or frame-shifting, generating polypeptides that were longer than expected (Fig. 6E). The G3U quadruplex also perturbed translation, causing the production of both longer and shorter polypeptides (Fig. 6E). The products of the expected size dominated when mutant RG4 regions were placed upstream of the stop codon, which indicated that the aberrant translation products were primarily the consequence of stable RG4 structures.

Discussion

The mammalian, yeast, and bacterial cells that we studied all strongly avoid the presence of folded RG4 structures in their transcriptomes but do so through different mechanisms. Based on our in vivo probing, the eukaryotic cells appear to have a robust and effective molecular machinery that specifically unfolds and maintains the thousands of RG4 regions in an unfolded state, whereas bacteria lack this machinery and have instead eliminated sequences with RG4-forming potential over the course of evolution. When considering the impaired growth rates observed for strains ectopically expressing RG4 regions, the bacterial mechanism is easy to

understand, but how might the eukaryotic mechanism act? Although the critical factors remain to be identified, this mechanism differs from that which unfolds Watson–Crick structure in two key aspects. First, it is less sensitive to ATP depletion, and second, it is more pervasive, unfolding essentially every RG4 that could be monitored in mESCs, MEFs and yeast, whereas the activities that unfold Watson–Crick structure allow many RNAs to remain folded.

We suspect that single-stranded RNA-binding proteins lie at the center of the mechanism that unfolds most eukaryotic RG4 regions. A wide variety of abundant RNA-binding proteins bind to G-rich RNA, including the hnRNP F/H family (28, 29), hnRNP D0 (30), hnRNP M (31), hnRNP A/B (32), hnRNP A1 (33, 34), hnRNP A2 (35), CBF-A (35), and SRSF1/2 (36). The solution structures of the three quasi-RNA recognition motifs (qRRMs) of hnRNP F in complex with G-tract RNA show how qRRMs could maintain G-tracts in a single-stranded conformation without blocking solvent accessibility to the N7 positions (37), which is consistent with our DMS probing results. Regardless of the identity of the machinery that operates in eukaryotic cells, it must be acting broadly throughout the transcriptome, including on untranslated RNAs and nuclear RNAs, as illustrated by the unfolding of RG4 regions within *Malat1* (Fig. 3C), a nuclear noncoding RNA.

The evolutionary depletion of RG4 regions might be more tenable for bacteria than for eukaryotes for two reasons. First, maintaining machinery dedicated to the remodeling of RG4s would be more costly for species under greater selective pressure to minimize their genomes. Second, species with smaller genomes would face less frequent de novo emergence of new RG4 regions. On the other hand, the eukaryotic mechanism provides opportunities for regulation. Indeed, the relative enrichment of RG4-forming regions in untranslated regions hints at the possibility that RG4 regions might be allowed to fold and impart regulatory functions in certain

cell types/states or subcellular compartments (38). Alternatively, these regions might impart function through transient folding that cannot be detected in our steady-state measurements. Another possibility is that the previously reported regulatory roles of RG4 regions, such as translational repression by RG4 regions within 5' UTRs (10), might result from the stable association of the RNA-binding proteins that maintain the RG4 regions in the unfolded state. In this scenario, the bound proteins rather than a folded RG4 would inhibit translation initiation. Clearly, more needs to be learned about this RNA structure in its native cellular contexts, and our results and methods provide the framework for doing so.

Acknowledgements

We thank S. Rouskin and members of the Bartel lab for helpful discussions, C. Kayatekin, G. Johnson, and K. Heindl for experimental assistance, J. S. Yoo, T. Fujita and Y. Nagamine for the *Dhx36* cell lines, S. Chisholm, S. Biller, and K. Dooley for the *Synechococcus* culture. This work was supported by NIH grant GM118135 (D.P.B.). J.U.G. is a Damon Runyon Fellow supported by the Damon Runyon Cancer Research Foundation (DRG-2152-13). D.P.B. is an investigator of the Howard Hughes Medical Institute. Sequencing data were deposited in GEO (accession number GSE83617).

Materials and Methods

In vivo DMS modification

DMS (Sigma-Aldrich; 50% diluted with ethanol) was added to mESCs or HEK293T cells cultured in 15 cm dishes to a final concentration of 8%, and evenly distributed by slow swirling. After incubating at 37°C for 5 minutes, the media and excess DMS were decanted, and cells

were washed twice with 25% β -mercaptoethanol (Sigma-Aldrich) in PBS to quench any residual DMS. After washing, cells were lysed in 10 mL TRIzol reagent (Invitrogen) supplemented with 5% β -mercaptoethanol, and lysates were stored at -80°C . DMS was added to 10 ml of yeast culture to a final concentration of 8%. After incubating at 30°C with continuous shaking for 5 minutes, two volumes of 25% β -mercaptoethanol were added to the culture to stop the modification. Cells were harvested by centrifugation at 4,000 rpm for 5 minutes and washed with 25% β -mercaptoethanol until no residual DMS was observed at the bottom of tubes. After the final centrifugation, cells were resuspended in RNAlater solution (Invitrogen) and stored at -80°C . DMS treatment of the *E. coli* culture was similar to that of the yeast culture, except it was performed at 37°C . For additional details on culture of and transfection of mammalian cells, culture and induction of yeast cells, culture and induction of bacteria, and construction of RG4 expression constructs, see the supplementary materials (SM).

In vitro folding and DMS modification

Poly(A)-selected RNA in 1 mM Mg^{2+} and 50 mM Tris-Cl (pH 7.0), either with or without 150 mM K^{+} , was heated to 80°C for 2 minutes and then rapidly cooled to 0°C for 1 minute. DMS was added to a final concentration of 8% and the mixture was incubated at either 37°C (mammalian and *E. coli* RNA) or 30°C (yeast RNA) for 5 minutes with constant mixing. Two volumes of 25% β -mercaptoethanol were added to stop the reaction before RNA was phenol-chloroform extracted and precipitated. For details on RNA purification, see SM.

RT-stop profiling

The DMS-seq protocol (7) was adapted to detect RT stops in unmodified RNA. 1 μ g poly(A)-selected RNA in 10 mM Tris-Cl (pH 7.5) was denatured at 95°C for 2 minutes, supplemented with RNA-fragmentation reagent (Ambion) and incubated at 95°C for additional 1 minute before adding EDTA stop solution (Ambion). After ethanol precipitation, RNA fragments were dephosphorylated at their 3' ends using T4 polynucleotide kinase (New England BioLabs). 60–80-nt RNA fragments were gel-purified and ligated to a pre-adenylated 3' DNA adapter (AppTCGTATGCCGTCTTCTGCTTGddC) using T4 RNA ligase 1 (New England BioLabs) without ATP. Products of the expected size (82–102 nt) were gel-purified and resuspended in 6 μ l water. For reverse transcription, 1 μ l 0.2 M Tris-Cl (pH 7.5), 1 μ l 1.5 M KCl (or NaCl or LiCl), 0.5 μ l 60 mM MgCl₂, 0.5 μ l 10 mM dNTP mix and 0.5 μ l 1 μ M 5' -radiolabeled primer (³²P-NNNNNGATCGTCGGACTGTAGAACTCTGAACCTGTCG/iSp18/CAAGCAGAAGACGGCATACG, in which N is any nucleotide, and iSp18 is an 18-atom hexa-ethyleneglycol spacer, IDT) were added to the RNA template. The mixture was incubated at 80°C for 2 minutes then cooled down to 42°C and incubated for additional 2 minutes before adding 100 U SuperScript III reverse transcriptase (Invitrogen). After incubation at 42°C for 10 minutes, the reaction was stopped with addition of 1 μ l 1 M NaOH, and the mixture was heated at 98°C for 15 minutes to hydrolyze the RNA. cDNAs from extension that stalled after addition of 20–45 nt were separated from primers and full-length cDNAs on a 10% urea gel, eluted and precipitated. Purified cDNA fragments were circularized using 50 U CircLigase (Epicentre) at 60°C for 4 hours before inactivation at 80°C for 10 minutes. Circularized cDNAs were amplified using a 5' indexed primer (AATGATACGGCGACCACCGACAGGTTGGAATTCTCGGGTGCCAAGGAAGTCCAGTC

ACxxxxxxATCCGACAGGTTCTACAGTCCGA, in which xxxxxx is the multiplexing index), a common 3' primer (CAAGCAGAAGACGGCATACGA), and Platinum Taq DNA Polymerase High Fidelity (Invitrogen) for 10–13 cycles of PCR. Libraries were purified on an 8% formamide gel and sequenced on a HiSeq 2000 sequencing machine (Illumina; 40 cycles, single-end mode). For details on transcript-specific analyses of model RG4 regions using primer-extension assays, see SM.

Analysis of sequencing reads

For each read that uniquely mapped to the cognate transcriptome, the nucleotide immediately upstream of the first aligned position was annotated as an RT stop. At each position of the transcriptome with ≥ 3 RT-stop reads, a fold-enrichment value (f) for RT stops was calculated as the ratio between the number of reads stalled at that position and the background read density, which was the average number of reads over all positions of the same nucleotide within the same transcript (e.g., all G nucleotides). RT stops with ≥ 10 reads and fold enrichment values ≥ 20 were designated strong stops (fig. S1). When calculating the fold enrichment values for negative-control samples (Li^+ , Na^+ , and 95°C DMS), the position under consideration was assigned a pseudo read count of 1 if it had no RT-stop reads (with no change to the background read density). Strong RT stops for which enrichment decreased by more than 50% in 150 mM Na^+ compared to 150 mM K^+ were designated K^+ -dependent. For details on read mapping, see SM.

NAI probing

NAI was synthesized as described (22) and stored as a 1M solution in DMSO at -80°C . For treatment in vivo, mESCs and yeast cells were treated with 80 mM NAI for 15 minutes at 37°C

and 30°C, respectively, and washed three times with PBS before RNA extraction and poly(A) selection. For treatment in vitro, poly(A)-selected RNA in 1 mM Mg²⁺ and 50 mM Tris-Cl (pH 7.0), either with or without 150 mM K⁺, and was heated to 80°C for 2 minutes and then rapidly cooled to 0°C for 1 minute. This refolded RNA was treated with 80 mM NAI for 5 minutes at either 37°C (mammalian RNA) or 30°C (yeast RNA). After treatment, RNA was phenol-chloroform extracted and precipitated. NAI-treated RNA was subjected to RT-stop profiling, using 150 mM Na⁺ instead of 150 mM K⁺ during primer extension. Gini coefficients were calculated for each non-overlapping RG4-containing region (identified as 60-nt regions upstream of K⁺-dependent strong RT stops) as

$$Gini = \frac{\sum_{i=1}^n \sum_{j=1}^n |r_i - r_j|}{2n^2 \bar{r}},$$

where n denotes the number of G residues in the RG4 region, and r_i denotes the RT-stop read number at position i .

Calculation of in vivo folding scores

For each RG4 region that retained a strong RT-stop signal (10 fold above background) when treated with DMS in the presence of K⁺ in vitro and had at least a 50% reduction in that signal when K⁺ was excluded, an in vivo folding score (s) was calculated as

$$S = \frac{f(\text{in vivo}) - f(\text{in vitro}; 0 \text{ mM K}^+)}{f(\text{in vitro}; 150 \text{ mM K}^+) - f(\text{in vitro}; 0 \text{ mM K}^+)}.$$

For the regions that had ≥ 100 RT-stop reads at G nucleotides after NAI probing and a difference of ≥ 0.1 in Gini coefficients when comparing results of RNA folded in vitro with K⁺ to those of RNA folded in vitro without K⁺, an in vivo folding score (s) was calculated as

$$S = \frac{Gini(\text{in vivo}) - Gini(\text{in vitro}; 0 \text{ mM K}^+)}{Gini(\text{in vitro}; 150 \text{ mM K}^+) - Gini(\text{in vitro}; 0 \text{ mM K}^+)}.$$

Although folding scores were calculated using linear functions, the conclusions of this study were not dependent on a linear relationship between the fraction of folded molecules and the extent of DMS or NAI modification.

Figure Legends

Fig. 1. Strong RT stops at G-rich regions in the mESC transcriptome. **(A)** The RNA G-quadruplex. The schematic (*left*) depicts a three-tiered RG4, with a parallel RNA-backbone orientation (solid line) and three G-quartets stabilized by two K⁺ ions (spheres). The chemical structure of a G-quartet (*right*) highlights hydrogen bonding (dashed lines) to the N7 positions (red) and K⁺-facilitated convergence of the exocyclic oxygens of the four G residues (R, ribose). **(B)** Schematic of RT-stop profiling. See text for explanation. **(C)** RT-stop profiles for *Eef2* mRNA (box, coding sequence) and *Malat1*. Bars representing each RT stop are colored according to the identity of the template nucleotide at the stall (position 0). Also shown for each transcript is the 40-nt RNA segment ending at the strongest stop. **(D)** Fraction of RT stops observed at each nucleotide, comparing all RT stops with only strong RT stops. **(E)** Nucleotide composition of the flanking sequences of strong RT stops at G. The direction of cDNA synthesis is indicated (arrow), with the 3' -terminal cDNA nucleotide assigned position +1. Template nucleotides are plotted at heights indicating the information content of their enrichment (bits).

Fig. 2. Folded RG4 structures cause strong RT stops. **(A)** RT-stop profiles of *Eef2*, showing enrichment observed in the original conditions (K⁺) and that observed when either substituting the monovalent cation used during RT (Li⁺ or Na⁺) or treating the RNA with DMS under denaturing conditions prior to RT (DMS 95°C). At each position within the mRNA, the fold enrichment was calculated as the number of RT-stop reads observed at that position, divided by the average number of RT-stop reads observed for all the mRNA positions with the same nucleotide identity. **(B)** Global analyses of strong RT stops, comparing the enrichment of stops observed in the original conditions (untreated; K⁺) to those observed when either substituting K⁺

with Na^+ (*top*) or pretreating RNA with DMS at 95°C (*bottom*). RT-stop values are colored according to the template nucleotide at position 0. The distributions are truncated at the left because stops with <20 fold enrichment in the untreated K^+ sample were not classified as strong stops. (C) Overlap between K^+ -dependent and DMS-sensitive strong RT stops (yellow and blue, respectively). (D) Abundance of RG4 regions within mRNA translated and untranslated regions. The expected abundances were estimated based on the relative number of G nucleotides within these three regions of detected mRNAs.

Fig. 3. RG4 regions are unfolded in mESCs. (A) Schematic of transcriptome-wide probing of RG4 folding. (B) Probing RG4 folding in vitro. The RT-stop enrichment observed after DMS treatment of RNA folded in K^+ (150 mM K^+) was compared to that observed after DMS treatment of RNA folded without K^+ (0 mM K^+). Values for regions with differences of ≥ 2 fold are indicated (blue). (C) RT-stop profiles of *Eef2* and *Malat1*, showing results observed after DMS treatment in vitro, either with or without K^+ , and those observed after DMS treatment in vivo. RT-stop enrichment values corresponding to RG4 regions are in blue; values for other RT stops at G nucleotides are in gray. In vivo folding scores for the RG4 regions are shown. (D) The distribution of in vivo folding scores of the 1,141 mESCs RG4 regions that were examined. The 0 and 1 reference values, which represent the signal observed when treating with DMS in vitro after folding with or without K^+ (panel B), are marked (dashed lines). (E) Distribution of in vivo folding scores observed for RG4 regions after either treating the cells with $2\ \mu\text{M}$ PDS for 24 hrs (PDS, red) or mock treatment (control, black). *, $p < 10^{-8}$, paired t-test. (F) Gene-specific primer extension of the ectopically expressed G3A2 quadruplex probed in vitro (after folding in either 0 or 150 mM K^+) or in vivo. Shown is a phosphorimage of a denaturing gel that resolved the

extension products of a P^{33} -radiolabeled primer. In the stop control, the β -mercaptoethanol quench was added to cells before DMS. The stronger RT stops are colored according to the nucleotide at the stall (A, red; C, orange; G, blue). The RG4 region is indicated (vertical line). For additional controls and sequencing ladders, see fig. S6E.

Fig. 4. RG4 regions are unfolded in *S. cerevisiae*. **(A)** Probing in vitro folding of yeast RG4s. Otherwise, as in Fig. 3B. **(B)** RT-stop profiles of *YPR088C*. Otherwise, as in Fig. 3C. **(C)** The distribution of in vivo folding scores of the 31 RG4 regions that were examined in yeast. Otherwise, as in Fig. 3D. **(D)** Gene-specific primer extension of the ectopically expressed G3A2 quadruplex probed in vitro (after folding in either 0 or 150 mM K^+) or in vivo. The primer was labeled with P^{32} ; otherwise, as in Fig. 3F.

Fig. 5. Probing RG4 folding using NAI. **(A)** Gene-specific primer extension of the ectopically expressed G3A2 quadruplex probed with NAI in vitro (after folding in either 0 or 150 mM K^+) or in yeast. Shown is a phosphorimage of a denaturing gel that resolved the extension products of a P^{32} -radiolabeled primer. RT stops corresponding to the preferential modifications of NAI within the G3A2 quadruplex are indicated (blue dots). **(B)** Schematic of transcriptome-wide probing of RG4 folding using NAI. **(C)** RT-stop profiles of an RG4 and its flanking regions within the *Eef2* 3' UTR, showing raw read counts colored according to the identity of the template nucleotide at the stall (position 0). G residues preferentially modified after folding in K^+ are indicated (blue arrowheads). **(D)** Comparison of Gini coefficients of the 310 RG4 regions with ≥ 100 RT stop reads in each of the two samples probed with NAI in vitro after folding in either 0 or 150 mM K^+ . Values for regions with differences of ≥ 0.1 between the two samples are indicated (blue). **(E)**

Distribution of in vivo folding scores of the 49 RG4 regions that were examined using NAI probing. Otherwise, as in Fig. 3D.

Fig. 6. RG4 folding and interference with growth and translation in *E. coli*. **(A)** Density of RG4 regions in bacterial and mESC transcriptomes. For each species, the number of RG4 regions, as identified from K⁺-dependent strong RT stops at G nucleotides, was normalized to the total length of all detected transcripts. **(B)** RT-stop profiles of an ectopically expressed *mCherry* mRNA with an G3A2 quadruplex inserted into its 3' UTR, showing results observed after DMS treatment in vitro, either with or without K⁺, and in vivo. Otherwise, as in Fig. 3C. **(C)** Gene-specific primer extension of ectopically expressed G3A2 (*left*, P³³-labeled primer) and G3U (*right*, P³²-labeled primer) quadruplexes probed with DMS. Otherwise, as in Fig. 3F. **(D)** Growth curves of strains expressing *mCherry* transcripts with the indicated RG4 (G3A2 or G3U) or RG4 mutant (G3A2m or G3Um) in either the 3' UTR (*left*) or the CDS (*right*). Growth was monitored using optical density at a wavelength of 600 nm (OD₆₀₀). Plotted are mean values ± SD (*n* = 6). *, *p* < 0.05; *** *p* < 0.001; Student's *t* tests using measurements at the last time point. **(E)** Immunoblot probed for the translation products of the *mCherry* constructs with either the indicated RG4 or its respective mutant inserted between the *mCherry* sequence and the stop codon. Mobilities of molecular-weight markers and the full-length products are shown.

Supplementary Materials

Materials and methods

Figures S1-S9

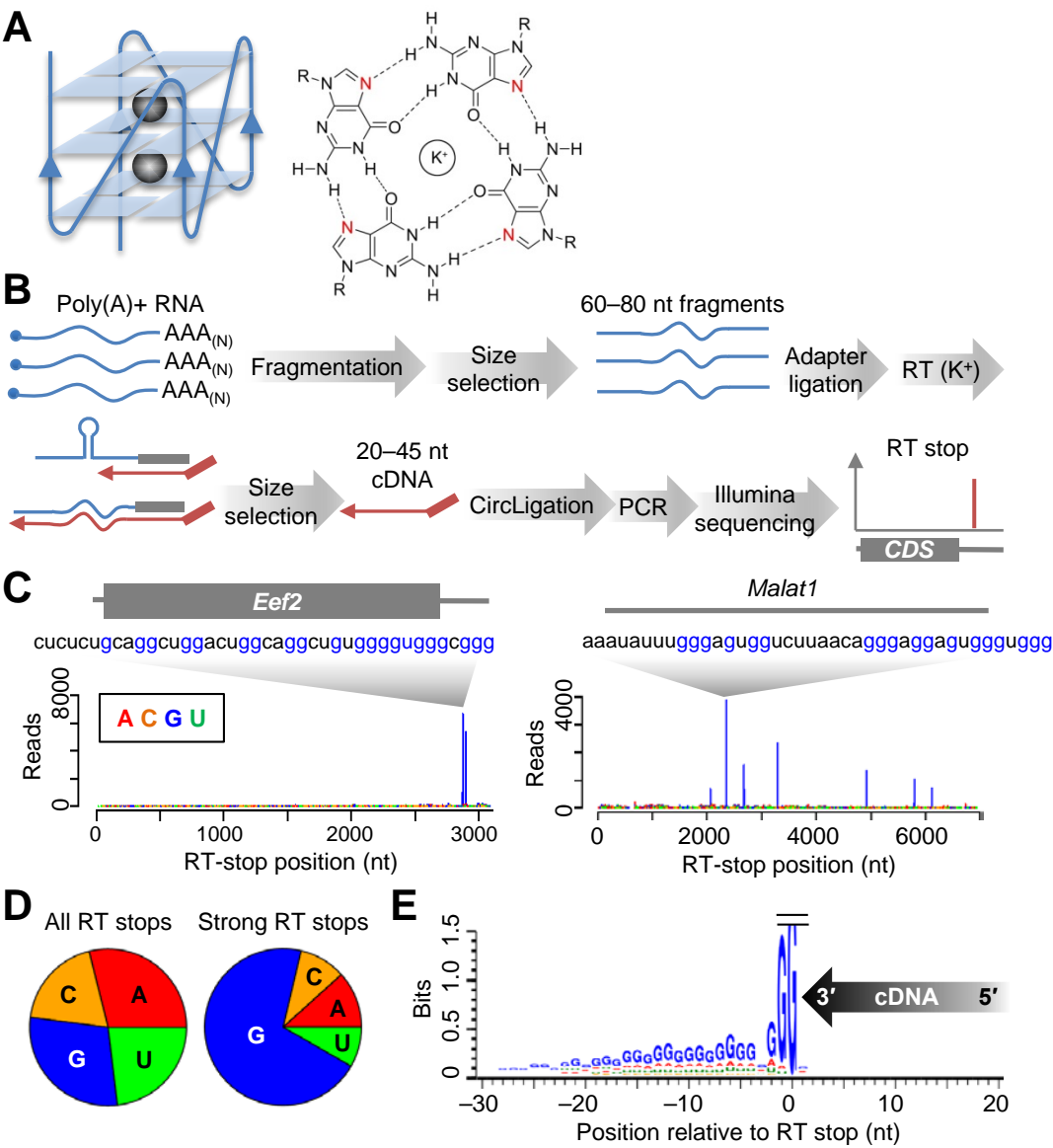
Reference (39–41)

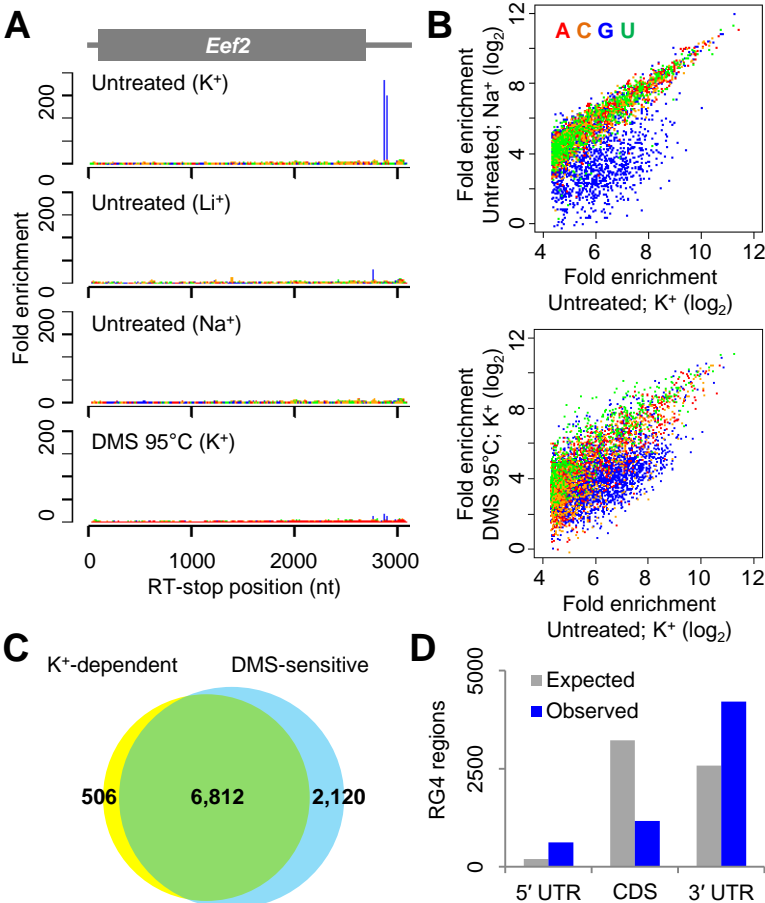
Tables S1-S6

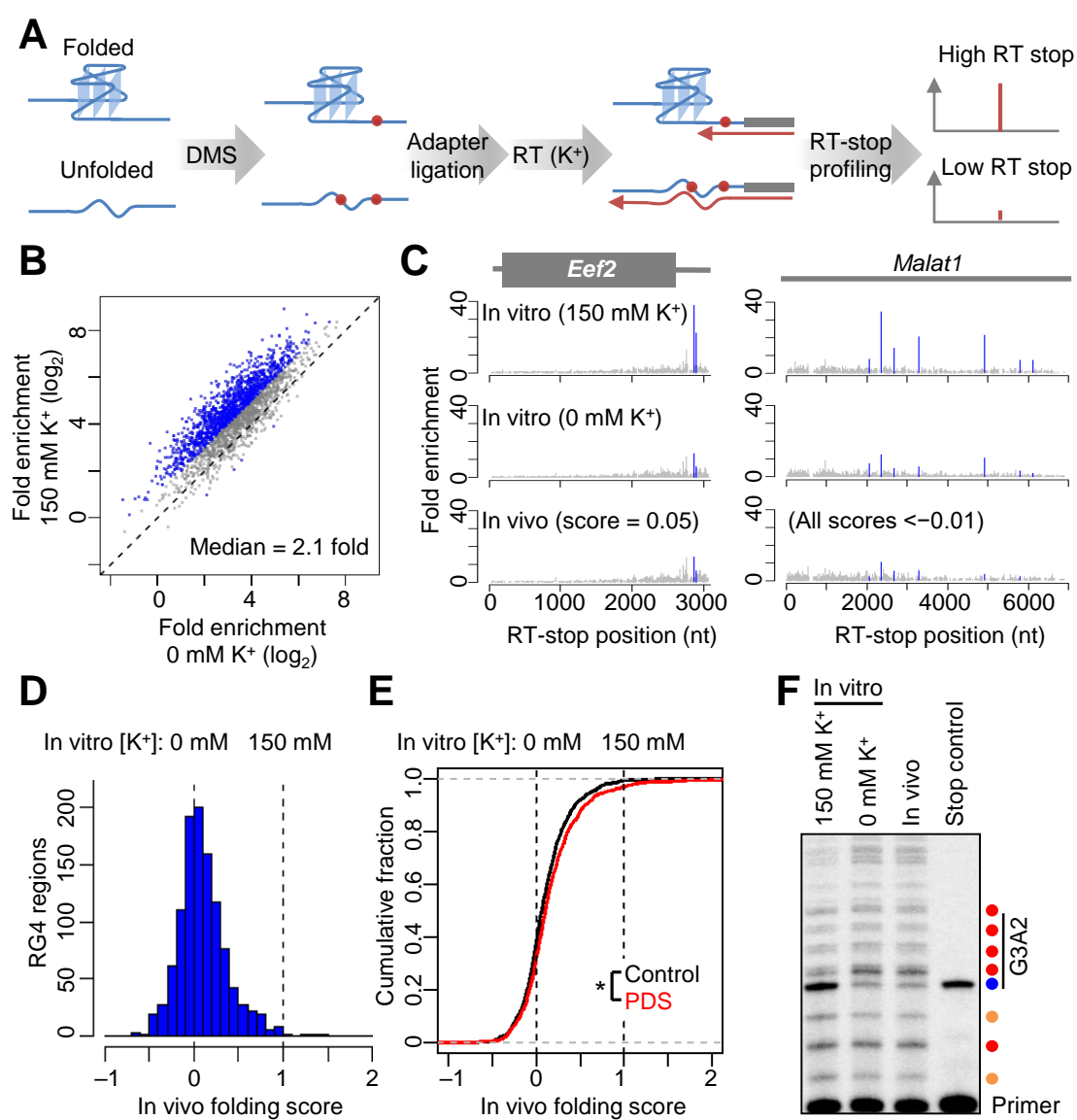
References and Notes

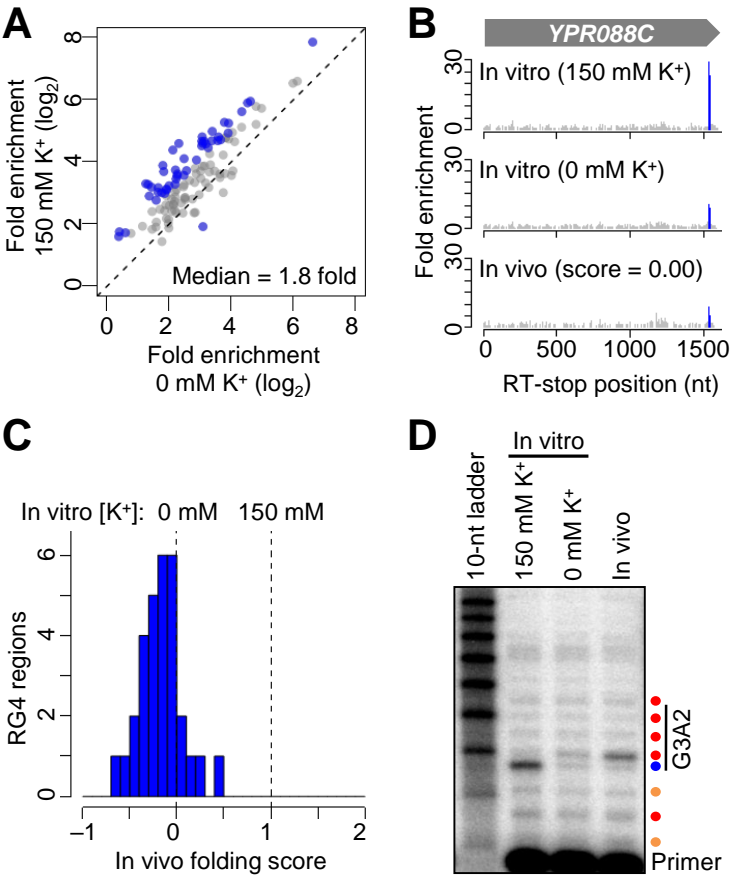
1. S. A. Mortimer, M. A. Kidwell, J. A. Doudna, Insights into RNA structure and function from genome-wide studies. *Nat Rev Genet* **15**, 469 (Jul, 2014).
2. Y. Wan, M. Kertesz, R. C. Spitale, E. Segal, H. Y. Chang, Understanding the transcriptome through RNA structure. *Nat Rev Genet* **12**, 641 (Sep, 2011).
3. K. M. Weeks, Advances in RNA structure analysis by chemical probing. *Curr Opin Struct Biol* **20**, 295 (Jun, 2010).
4. S. E. Wells, J. M. Hughes, A. H. Igel, M. Ares, Jr., Use of dimethyl sulfate to probe RNA structure in vivo. *Methods Enzymol* **318**, 479 (2000).
5. M. Kubota, C. Tran, R. C. Spitale, Progress and challenges for chemical probing of RNA structure inside living cells. *Nat Chem Biol* **11**, 933 (Dec, 2015).
6. Y. Ding *et al.*, In vivo genome-wide profiling of RNA secondary structure reveals novel regulatory features. *Nature* **505**, 696 (Jan 30, 2014).
7. S. Rouskin, M. Zubradt, S. Washietl, M. Kellis, J. S. Weissman, Genome-wide probing of RNA structure reveals active unfolding of mRNA structures in vivo. *Nature* **505**, 701 (Jan 30, 2014).
8. D. Loughrey, K. E. Watters, A. H. Settle, J. B. Lucks, SHAPE-Seq 2.0: systematic optimization and extension of high-throughput chemical probing of RNA secondary structure with next generation sequencing. *Nucleic Acids Res* **42**, (Dec 1, 2014).
9. R. C. Spitale *et al.*, Structural imprints in vivo decode RNA regulatory mechanisms. *Nature* **519**, 486 (Mar 26, 2015).
10. A. Bugaut, S. Balasubramanian, 5'-UTR RNA G-quadruplexes: translation regulation and targeting. *Nucleic Acids Res* **40**, 4727 (Jun, 2012).
11. S. Millevoi, H. Moine, S. Vagner, G-quadruplexes in RNA biology. *Wiley Interdiscip Rev RNA* **3**, 495 (Jul-Aug, 2012).
12. A. L. Wolfe *et al.*, RNA G-quadruplexes cause eIF4A-dependent oncogene translation in cancer. *Nature* **513**, 65 (Sep 4, 2014).
13. A. R. Haeusler *et al.*, C9orf72 nucleotide repeat structures initiate molecular cascades of disease. *Nature* **507**, 195 (Mar 13, 2014).
14. G. Biffi, M. Di Antonio, D. Tannahill, S. Balasubramanian, Visualization and selective chemical targeting of RNA G-quadruplex structures in the cytoplasm of human cells. *Nat Chem* **6**, 75 (Jan, 2014).
15. C. K. Kwok, S. Balasubramanian, Targeted Detection of G-Quadruplexes in Cellular RNAs. *Angew Chem Int Ed Engl* **54**, 6751 (Jun 1, 2015).
16. D. A. Peattie, Direct chemical method for sequencing RNA. *Proc Natl Acad Sci U S A* **76**, 1760 (Apr, 1979).
17. M. Vorlickova *et al.*, Circular dichroism and guanine quadruplexes. *Methods* **57**, 64 (May, 2012).
18. J. L. Huppert, A. Bugaut, S. Kumari, S. Balasubramanian, G-quadruplexes: the beginning and end of UTRs. *Nucleic Acids Res* **36**, 6260 (Nov, 2008).
19. J. M. Garant, M. J. Luce, M. S. Scott, J. P. Perreault, G4RNA: an RNA G-quadruplex database. *Database (Oxford)* **2015**, (2015).
20. V. S. Chambers *et al.*, High-throughput sequencing of DNA G-quadruplex structures in the human genome. *Nat Biotechnol* **33**, 877 (Aug, 2015).

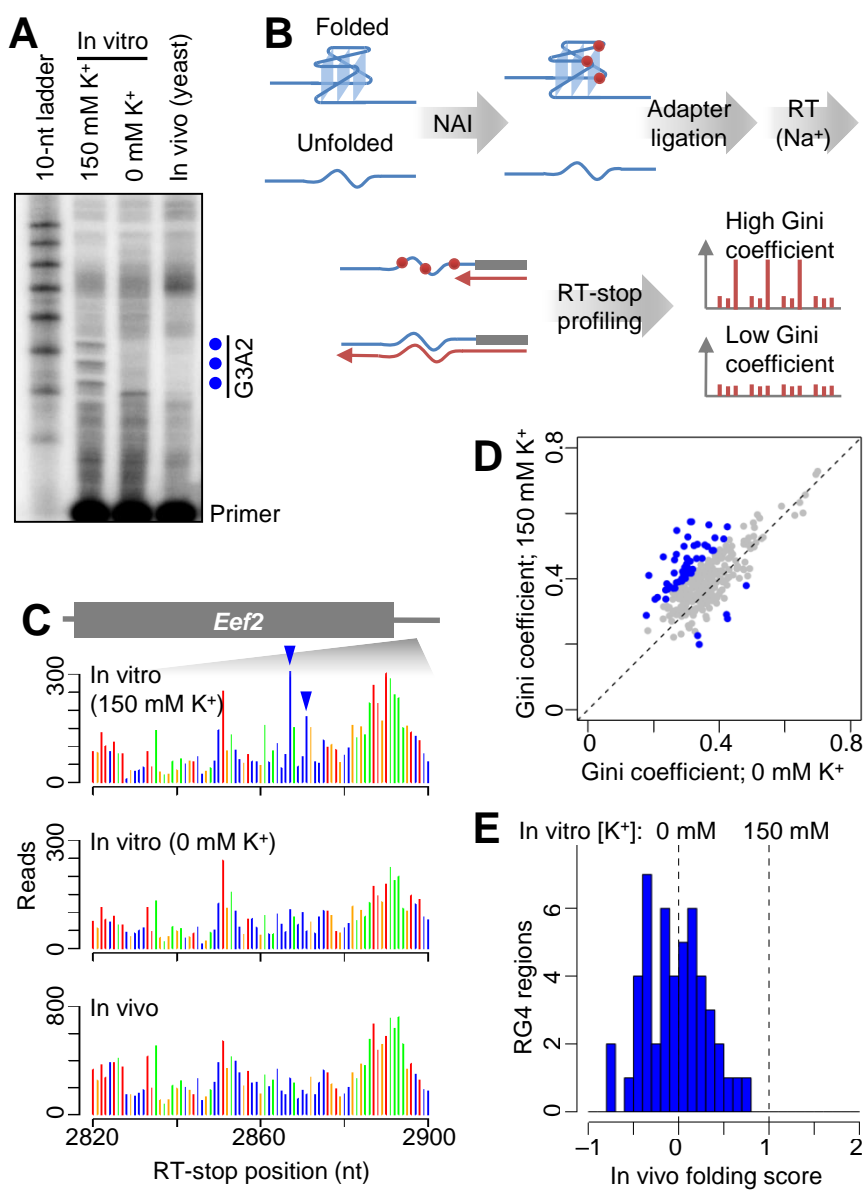
21. P. D. Lawley, P. Brookes, Further Studies on the Alkylation of Nucleic Acids and Their Constituent Nucleotides. *Biochem J* **89**, 127 (Oct, 1963).
22. R. C. Spitale *et al.*, RNA SHAPE analysis in living cells. *Nat Chem Biol* **9**, 18 (Jan, 2013).
23. C. K. Kwok, A. B. Sahakyan, S. Balasubramanian, Structural Analysis using SHALiPE to Reveal RNA G-Quadruplex Formation in Human Precursor MicroRNA. *Angew Chem Int Ed Engl* **55**, 8958 (Jul 25, 2016).
24. G. W. Collie, S. M. Haider, S. Neidle, G. N. Parkinson, A crystallographic and modelling study of a human telomeric RNA (TERRA) quadruplex. *Nucleic Acids Res* **38**, 5569 (Sep, 2010).
25. S. D. Creacy *et al.*, G4 resolvase 1 binds both DNA and RNA tetramolecular quadruplex with high affinity and is the major source of tetramolecular quadruplex G4-DNA and G4-RNA resolving activity in HeLa cell lysates. *J Biol Chem* **283**, 34626 (Dec 12, 2008).
26. J. S. Yoo *et al.*, DHX36 enhances RIG-I signaling by facilitating PKR-mediated antiviral stress granule formation. *PLoS Pathog* **10**, e1004012 (Mar, 2014).
27. I. T. Holder, J. S. Hartig, A matter of location: influence of G-quadruplexes on Escherichia coli gene expression. *Chem Biol* **21**, 1511 (Nov 20, 2014).
28. M. J. Matunis, J. Xing, G. Dreyfuss, The hnRNP F protein: unique primary structure, nucleic acid-binding properties, and subcellular localization. *Nucleic Acids Res* **22**, 1059 (Mar 25, 1994).
29. M. Caputi, A. M. Zahler, Determination of the RNA binding specificity of the heterogeneous nuclear ribonucleoprotein (hnRNP) H/H'/F/2H9 family. *J Biol Chem* **276**, 43850 (Nov 23, 2001).
30. T. Nagata *et al.*, Structure and interactions with RNA of the N-terminal UUAG-specific RNA-binding domain of hnRNP D0. *J Mol Biol* **287**, 221 (Mar 26, 1999).
31. K. V. Datar, G. Dreyfuss, M. S. Swanson, The human hnRNP M proteins: identification of a methionine/arginine-rich repeat motif in ribonucleoproteins. *Nucleic Acids Res* **21**, 439 (Feb 11, 1993).
32. A. Kumar, H. Sierakowska, W. Szer, Purification and RNA binding properties of a C-type hnRNP protein from HeLa cells. *J Biol Chem* **262**, 17126 (Dec 15, 1987).
33. Q. S. Zhang, L. Manche, R. M. Xu, A. R. Krainer, hnRNP A1 associates with telomere ends and stimulates telomerase activity. *Rna* **12**, 1116 (Jun, 2006).
34. C. G. Burd, G. Dreyfuss, RNA binding specificity of hnRNP A1: significance of hnRNP A1 high-affinity binding sites in pre-mRNA splicing. *Embo J* **13**, 1197 (Mar 1, 1994).
35. S. Khateb, P. Weisman-Shomer, I. Hershco-Shani, A. L. Ludwig, M. Fry, The tetraplex (CGG)_n destabilizing proteins hnRNP A2 and CBF-A enhance the in vivo translation of fragile X premutation mRNA. *Nucleic Acids Res* **35**, 5775 (2007).
36. A. Expert-Bezancon *et al.*, hnRNP A1 and the SR proteins ASF/SF2 and SC35 have antagonistic functions in splicing of beta-tropomyosin exon 6B. *J Biol Chem* **279**, 38249 (Sep 10, 2004).
37. C. Dominguez, J. F. Fisette, B. Chabot, F. H. Allain, Structural basis of G-tract recognition and encaging by hnRNP F quasi-RRMs. *Nat Struct Mol Biol* **17**, 853 (Jul, 2010).
38. M. Subramanian *et al.*, G-quadruplex RNA structure as a signal for neurite mRNA targeting. *EMBO Rep* **12**, 697 (Jul, 2011).

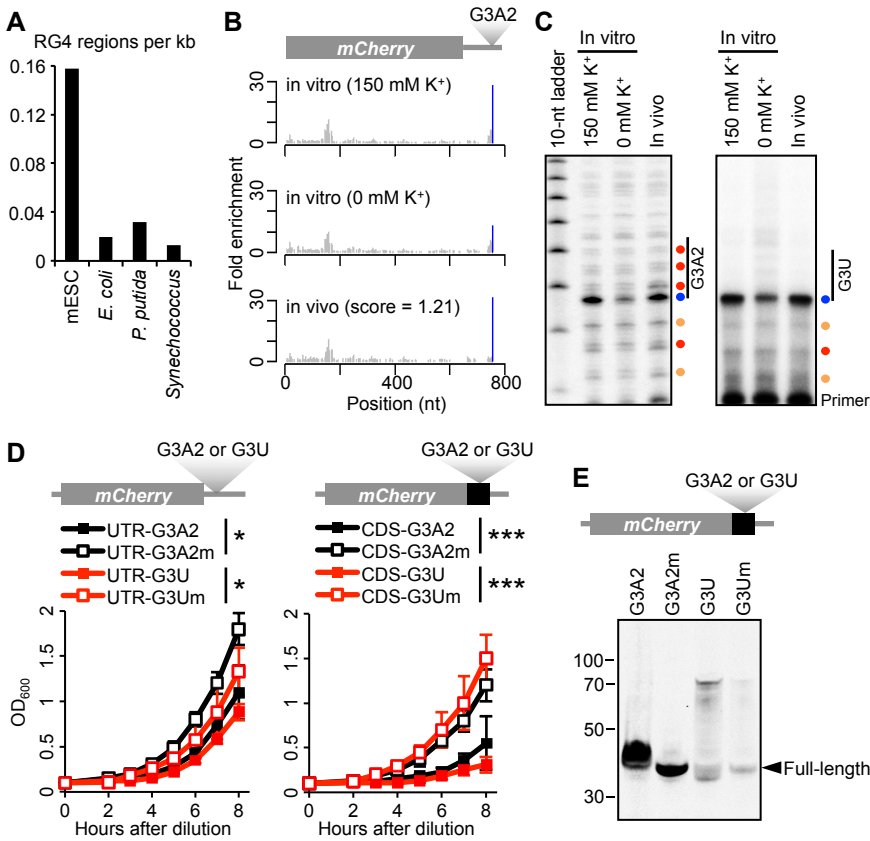












Supplemental Materials and Methods

Mammalian cell culture and transfection

Feeder-free mESCs were cultured on 0.1% gelatin-coated plates in DMEM (high glucose) supplemented with 1X nonessential amino acids (Invitrogen), 1X penicillin-streptomycin-glutamine (Invitrogen), 15% defined fetal bovine serum (HyClone-ES screened) and 1000 U/mL ESGRO leukemia inhibitory factor (Millipore). Adherent HeLa and HEK293T cells were cultured in DMEM (high glucose) supplemented with 10% fetal bovine serum. After splitting and culturing overnight to 70–90% confluence, 10 cm plates of HEK293T cells were each transfected with 10 µg pcDNA3-mCherry-G3A2 plasmid and 60 µl Lipofectamine 2000 (Invitrogen) according to the manufacturer's instructions.

Yeast culture and induction

S. cerevisiae strain yRH101 harboring the pYES2.1-mCherry-4x AAGGG plasmid was cultured at 30°C in SD-Ura media supplemented with 2% raffinose. For induced expression, an overnight culture was inoculated into SD-Ura media with 2% galactose at an OD₆₀₀ of 0.4 and allowed to grow for another 6 hours before harvest.

Bacterial culture and induction

For growth curves, overnight cultures of *E. coli* TOP10 strains harboring pCR2.1-mCherry plasmids with RG4 or mutant insertions were diluted to an OD₆₀₀ of 0.1 with LB supplemented with 100 µg/ml ampicillin and allowed to grow at 37°C with shaking. For induced protein expression, exponential-phase (OD₆₀₀ = 0.4–0.6) cultures of BL21 strains that overexpressed LacIq and harbored the plasmids were induced by addition of 0.5 mM IPTG and allowed to grow at 37°C for two hours before harvest. Frozen stock of *P. putida* strain KT2440 was obtained from ATCC (#47054). A single colony was picked from an LB/agar plate and cultured in LB broth at 37°C with shaking. A 400mL axenic culture of *Synechococcus* sp WH8102 was grown in natural seawater-based Pro99 media containing 0.2 µm filtered Sargasso Sea water amended with Pro99 nutrients, supplemented with 6 mM sterile sodium bicarbonate to support the growth of a large volume of culture (39). Cells were grown at 24 °C under constant illumination (45 µmol photons m⁻² s⁻¹) to mid-exponential growth phase.

RNA purification

Total RNA was extracted from mammalian cells using TRIzol (Invitrogen) according to the manufacturer's instructions. Yeast total RNA was extracted with hot acid phenol:chloroform:isoamyl alcohol (PCA, 25:24:1, Ambion) with 0.5% SDS and then ethanol precipitated. Poly(A)⁺ RNA was purified using oligo(dT) Dynabeads (Invitrogen) according to the manufacturer's instructions. To purify bacterial total RNA, cells were first treated with 2 mg/ml lysozyme (Sigma) for 2 minutes at room temperature before hot PCA/SDS extraction and precipitation. Ribosomal RNA was depleted using Ribo-Zero for Gram-negative bacteria (Epicenter).

Mapping of sequencing reads

The six random nucleotides of the RT primer reduced circLigase bias and enabled the removal of PCR-duplicated sequences. After removing these duplicates, the first six nucleotides and the 3'-adapter sequences were trimmed using FASTX tools. The trimmed sequences were aligned to either the *S. cerevisiae* transcriptome (Saccharomyces Genome Database, version 2015-1-13), non-redundant RefSeq-based mouse or human transcriptomes (available at bartellab.wi.mit.edu/publication.html), or RefSeq transcriptomes for *E. coli*, *P. putida* and *Synechococcus sp WH8102* using Bowtie, requiring unique mapping and allowing one mismatch.

Transcript-specific analyses using primer-extension assays

1 µl 0.2 M Tris-Cl (pH 7.5), 1 µl 1.5 M KCl or NaCl (for DMS probing and NAI probing, respectively), 0.5 µl 60 mM MgCl₂, 0.5 µl 10 mM dNTP mix and 0.5 µl 1 µM 5'-³²P or ³³P-labeled primer (^{32/33}p-CAAGCAGAAGACGGCATACG, IDT) were added to 5 µl RNA template (2 µg or 5 µg DMS-treated or NAI-treated poly(A)⁺ RNA, respectively). The mixture was incubated at 80°C for 2 minutes then cooled to 42°C and incubated for additional 2 minutes before adding 50 U SuperScript III reverse transcriptase (Invitrogen). After incubation at 42°C for 10 minutes, the reaction was stopped with addition of 1 µl 1 M NaOH, and the mixture was heated at 98°C for 15 minutes to hydrolyze the RNA. The mixture was neutralized with 1 µl 1M HCl, mixed with an equal volume of Gel Loading Buffer II (Ambion) and denatured at 85°C for 15 minutes. cDNAs were separated on a 8% urea gel. ³²P gels were frozen and imaged using a Typhoon Phosphoimager (GE). ³³P gels were fixed in 10% acetic acid and 10% methanol and dried at 80°C under vacuum (Bio-Rad gel dryer) before imaging.

RG4 expression constructs

The G3A2 quadruplex (underlined) was appended by PCR to the *mCherry* CDS (in bold) within the context of the following sequence:

...**TACAAGTAAATAGATTTGCGTTACTGTCTAAGGGAAGgGAAGgG**
AAGGGTTTTCTTTTATTTTCTTTTCGTATGCCGTCTTCTGCTTGAAAAA
 AAAAAAAAAAAAAAAAAAAAAA. This PCR product was inserted to expression vectors (pCR2.1 for *E. coli*, pYES2.1 for yeast, pcDNA3.1 for mammalian cells) by TOPO TA cloning (Life Technologies). The A₃₀ region enabled the enrichment of the transcript from total *E. coli* RNA using oligo(dT) beads. In G3U constructs, the underlined segment was replaced with TTTGgGTGgGTGGGTGGG. For stop-codon mutants, the TAA stop codon was replaced with AAA so that the CDS was extended to include the RG4 region before terminating at the downstream TGA codon (italicized). In G3A2 and G3U mutants, the middle G residues (small letters) in two of the four G tracts were mutated to A and U, respectively.

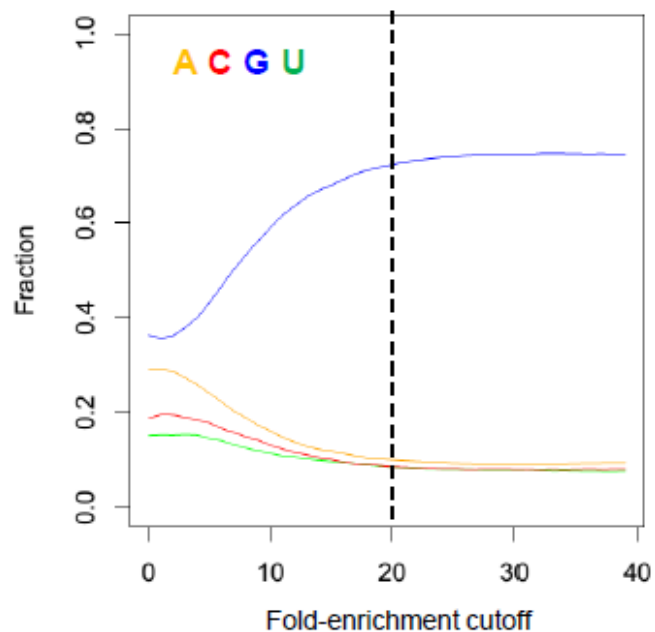


Fig. S1. Nucleotide composition at position 0 of RT stops of varying strength. At each fold-enrichment cutoff, the fraction of stops at the indicated nucleotide is plotted, considering only stops supported by ≥ 10 reads. Stops with enrichment of ≥ 20 fold (dashed line) were carried forward as strong RT stops.

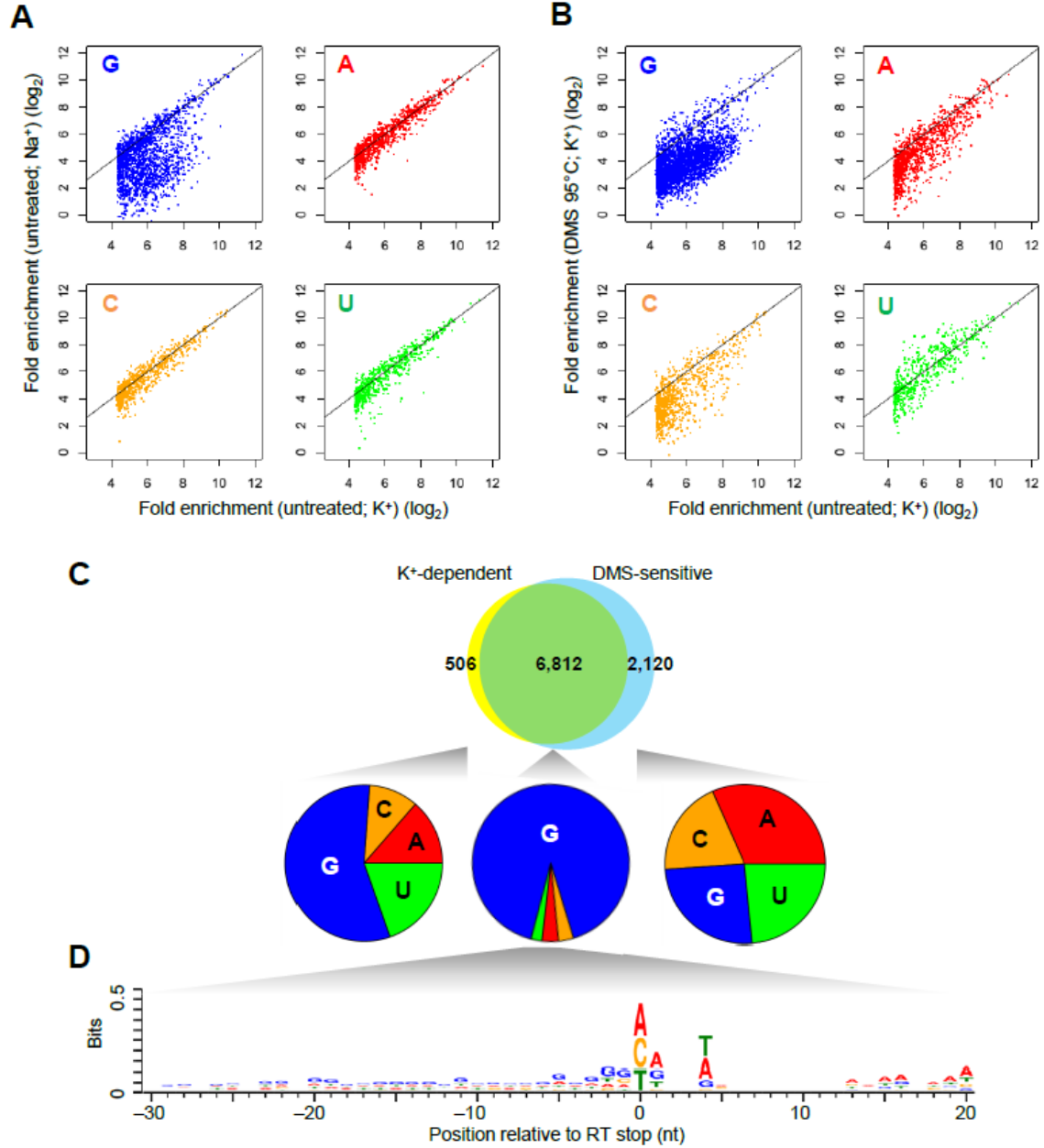


Fig. S2. K^+ -dependency and DMS-sensitivity of strong RT stops. **(A)** The results of the top panel of Fig. 2B, re-plotted to show the data for RT stops at each of the four nucleotides separately. **(B)** The results of the bottom panel of Fig. 2B. **(C)** Nucleotide composition at position 0 for RT stops that were either K^+ -dependent but DMS-insensitive (*left*), K^+ -dependent and DMS-sensitive (*middle*), or K^+ -independent but DMS-sensitive (*right*). **(D)** Nucleotide composition of the flanking sequences of 672 K^+ -dependent, DMS-sensitive strong RT stops that lacked a G at position 0. Nucleotides are plotted at heights indicating the information content of their enrichment (bits).

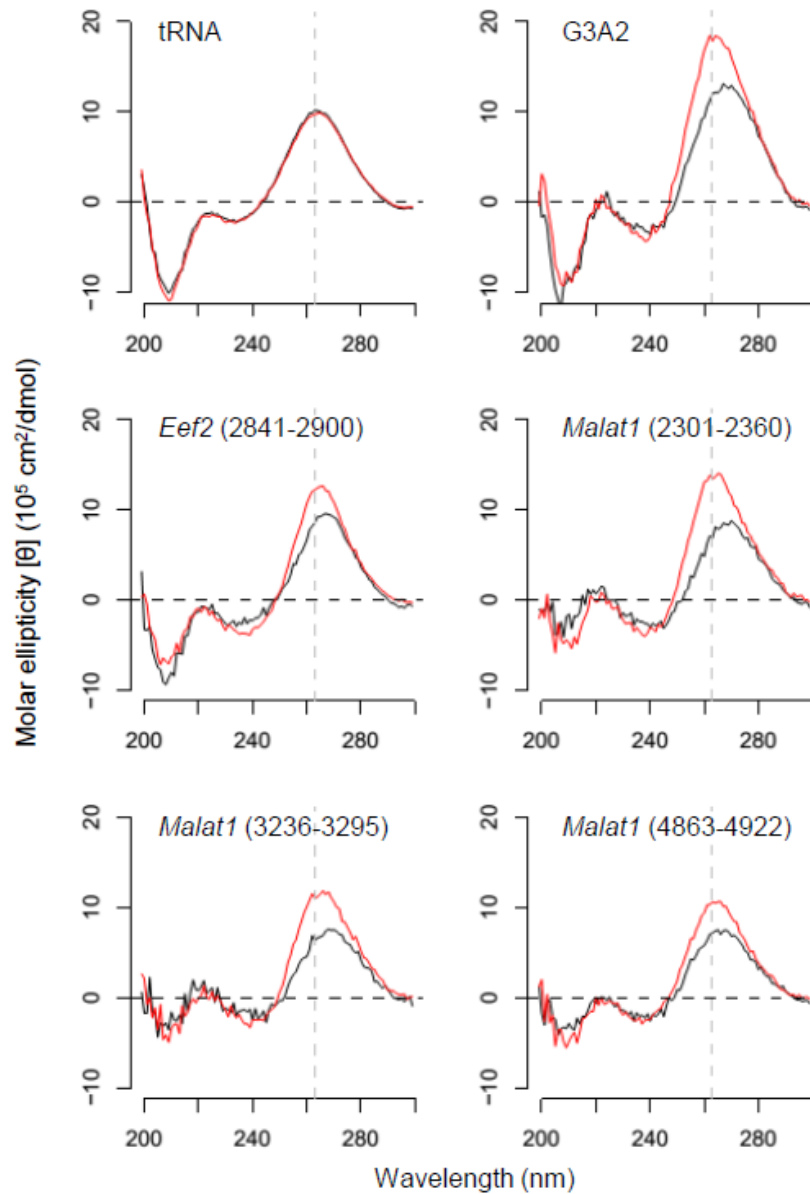


Fig. S3. Circular dichroism (CD) spectra of control RNAs (*E. coli* tRNA and the G3A2 quadruplex) and four 60-nt regions upstream of K⁺-dependent strong RT stops. Each RNA (4 μ M) was heat-denatured and allowed to fold at 42°C in 20 mM Tris-Cl (pH 7.5), 1mM MgCl₂ and either 150 mM (red) or 0 mM K⁺ (black). A K⁺-dependent increase in the positive peak at 263 nm (vertical dashed line), indicative of parallel RG4 structure formation, was observed in the G3A2 positive control and all four RG4 regions examined, but not in the tRNA negative control. The G3A2 RNA had the sequence GG ATAGATTTCGCTTACTGTCTAAGGGAAGGGAAGGGAAGGGTTTTCTTTTATT TTCTTTTCGTATGCCGTCTTCTGCTTG. The endogenous RG4 regions included the segments of *Eef2* and *Malat1* transcripts (NM_007907 and NR_002847, respectively) shown in parentheses. To facilitate efficient in vitro transcription, G residues were added to regions that did not already begin with GG at their 5' termini.

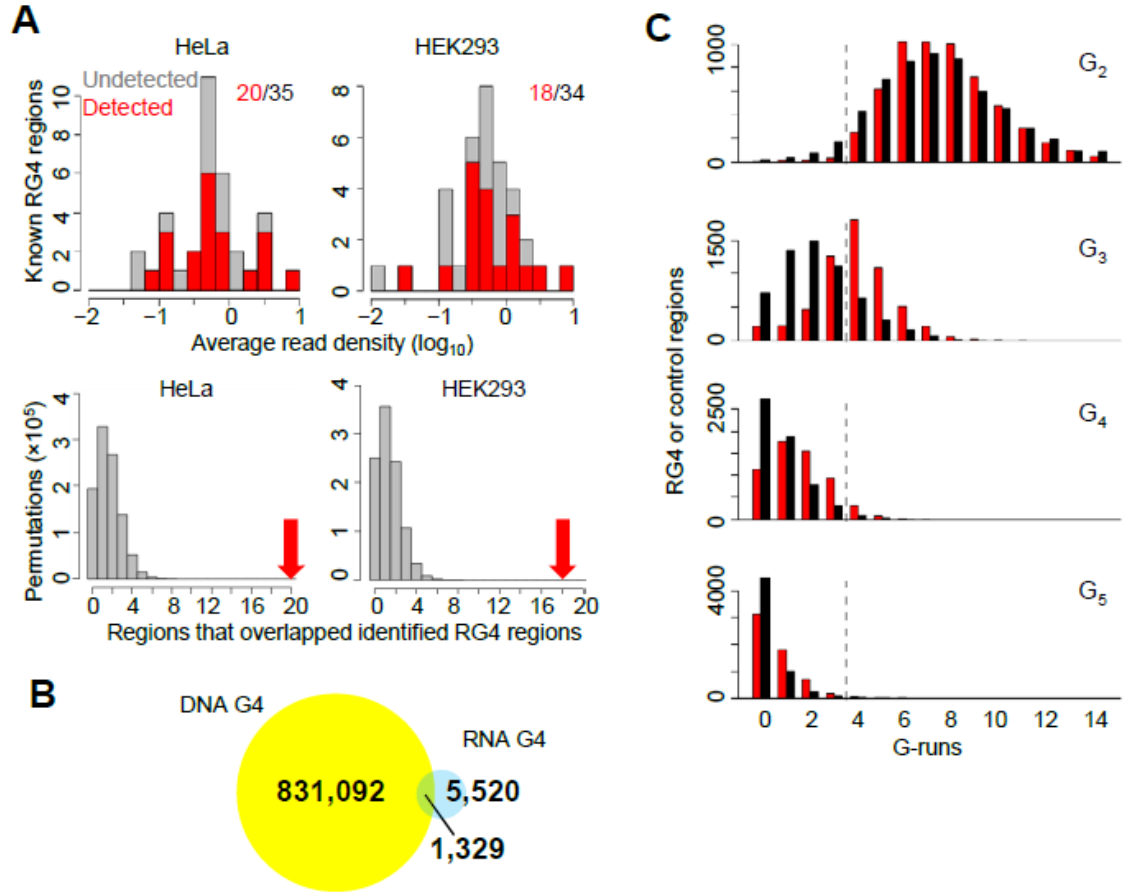


Fig. S4 . Characteristics of RG4 regions. **(A)** Overlap between the previously identified RG4 regions and those identified as K⁺-dependent RT stops. The upper panels plot the distribution of the average RT stop read densities of mRNAs with previously known RG4 regions in HeLa cells (*left*) and HEK293T cells (*right*), indicating in red those that overlapped the RG4 regions identified through RT-stop profiling (table S2). All mRNAs with at least one RT-stop read were considered. The lower panels show results of permutation tests using one million cohorts of length-matched randomly selected regions from mRNAs with at least one RT-stop read, showing chance overlap with the previously known regions. The numbers of previously known RG4 regions detected in the upper panels, indicated by red arrows, exceeded those of all permutations. The mean of all permutations, 1.7 and 1.3, respectively, implied false-discovery rates of 1.7/20 and 1.3/18, respectively. **(B)** Overlap between previously identified human genomic DNA G4 regions (20) and the set of 6,849 RG4 regions that were identified through RT-stop profiling of RNA from either HeLa or HEK293T cells, uniquely mapped to the reference genome, and did not overlap with each other. **(C)** Contiguous G-runs in RG4 regions. For continuous G-runs of the minimal lengths indicated (G₂ to G₅), the distribution of RG4 regions with the indicated numbers of runs is plotted (red), counting all non-overlapping runs (separated by ≥ 1 nucleotide) within 60 nt upstream of each RT stop. For comparison, the analysis was repeated with a control cohort of 60-nt mRNA regions with equivalent G content (black). For each of the four G-run lengths, RG4 regions had more continuous G-runs than did control regions ($p < 10^{-15}$, one-sided K-S test).

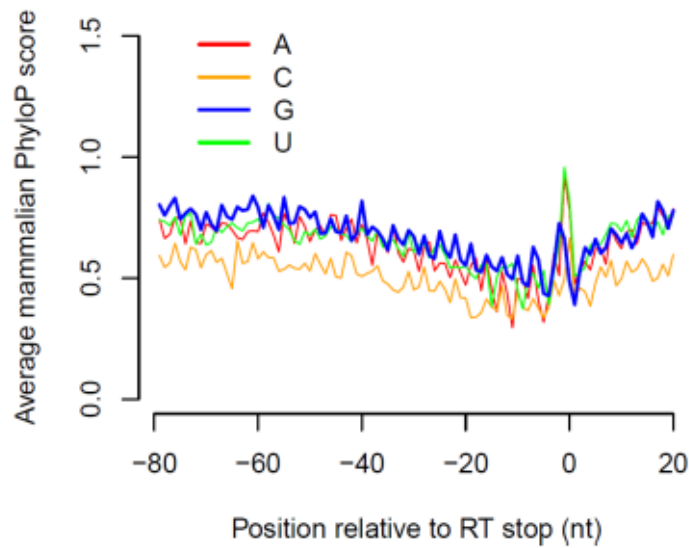


Fig. S5. Sequence conservation of the 6,857 RG4 regions identified in mESCs (table S1). For each of the four nucleotides, PhyloP scores (40) from the mouse-centric whole-genome alignments (UCSC Genome Browser, version 2014-07-24) were averaged at each position relative to K⁺-dependent strong RT stops. Overall, scores of the G residues resembled those of the A and U residues, and scores within the RG4 regions (positions -60 – 0) resembled those of the flanking regions.

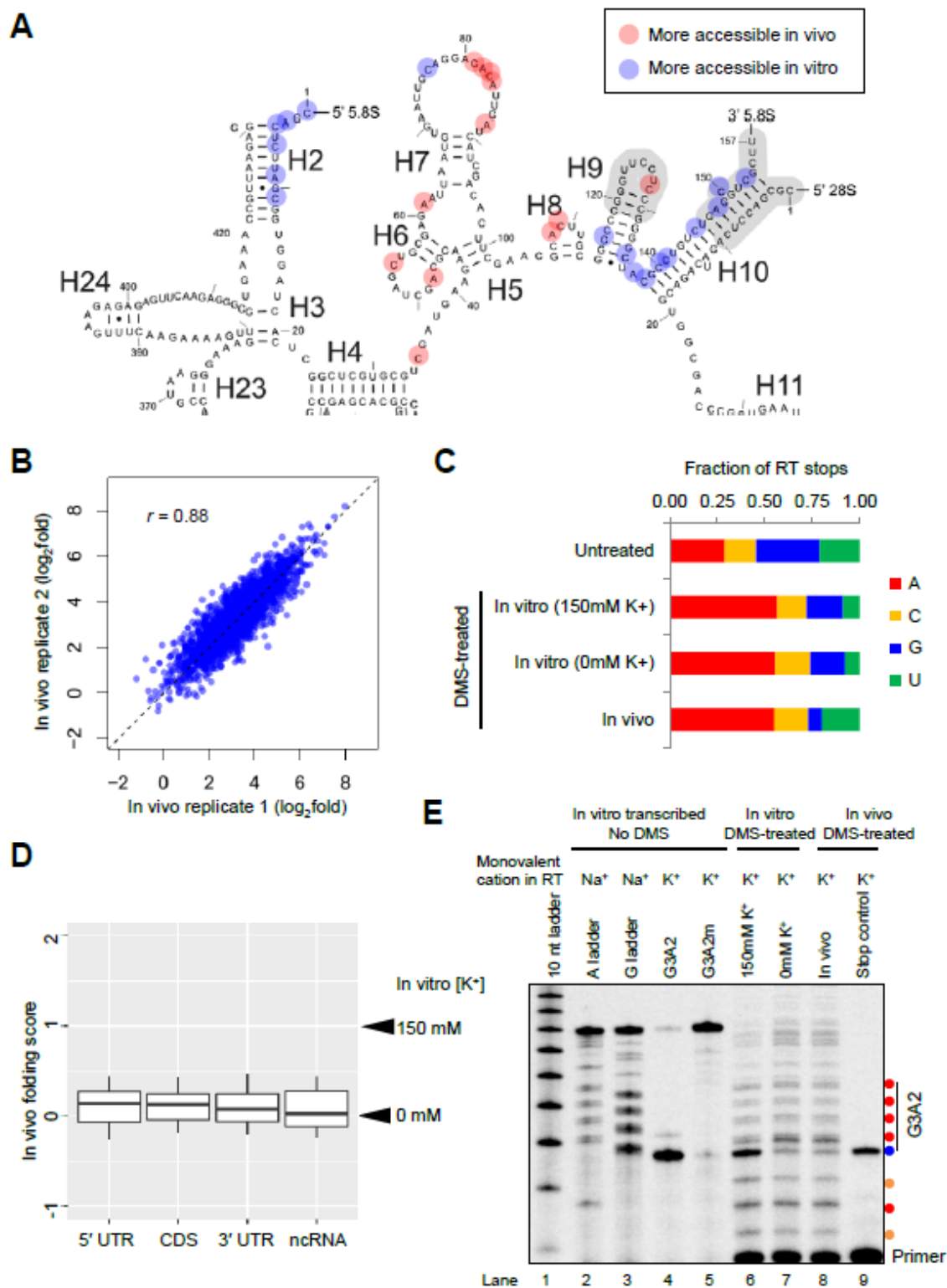


Fig. S6. In vivo DMS probing (*legend on next page*).

Fig. S6. In vivo DMS probing. **(A)** RT stops at A and C residues of 5.8S rRNA, comparing the results of treating ESCs with DMS to those of treating purified refolded RNA. Nucleotides that were ≥ 2 fold more accessible in vivo or in vitro are labeled in red or blue, respectively. **(B)** A comparison of fold-enrichment values from two biological replicates. For each replicate, mESCs were treated with DMS, and the mRNA was extracted and RT-stop profiled. Pearson's correlation coefficient (r) is shown. The data from these two replicates were combined in the following analyses. **(C)** The nucleotide identities at RT-stop reads from the untreated and DMS-treated samples. Note that the fraction of reads that stopped at A and C were similar across all DMS-treated samples. **(D)** In vivo folding of RG4 regions mapping to non-coding RNA (ncRNA) or different regions of mRNAs. Box plots indicate the distributions of in vivo folding scores (median, line; box, quartiles; whiskers 10th and 90th percentiles). In vitro reference levels are indicated. **(E)** The analysis of Fig. 3F, but showing additional lanes with markers and controls. Lanes 6–9 are the ones of Fig. 3F. Also shown is a marker lane (lane 1) and four lanes resolving RT products of in vitro transcribed versions of the RNA that contained the G3A2 quadruplex. Lanes 2 and 3 are A and G ladders, which were generated by including chain terminators (ddTTP or ddCTP, respectively) during RT reactions that were done in the presence of Na^+ instead of K^+ . Note that a stop from a chain terminator yields a product that is 1 nt longer than a stop at a RG4 or methylated A or C residue. Lanes 4 and 5 show that the strong RT stop normally observed at the G3A2 quadruplex (lane 4) was abolished when the G3A2 quadruplex was replaced with a mutant version (G3A2m) that contained two G-to-A point substitutions designed to disrupt the quadruplex (lane 5).

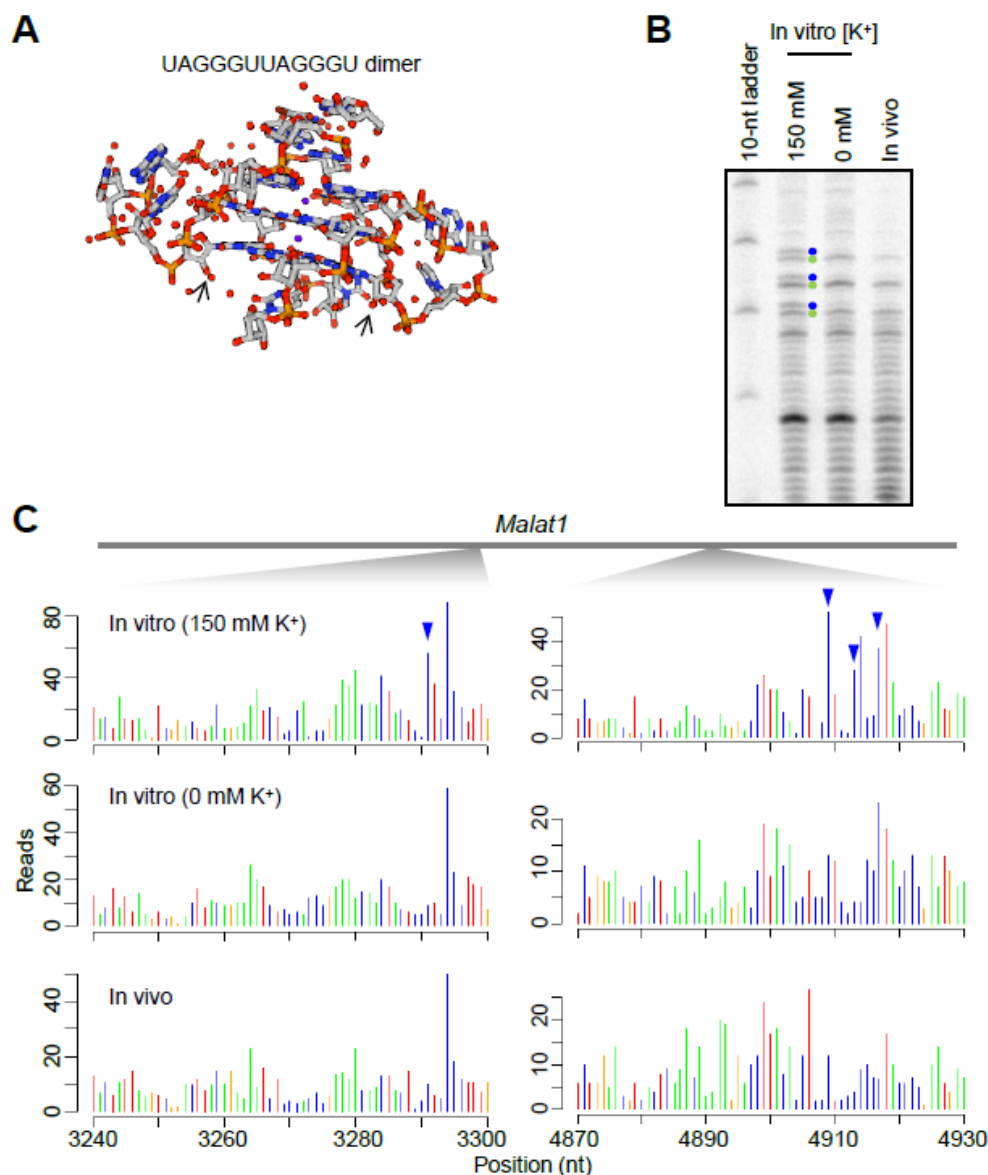


Fig. S7. Exposure of 2'-hydroxyl groups in a parallel RG4 structure. **(A)** The crystal structure of an intermolecular RG4 formed from two molecules of the indicated sequence (PDB accession: 3IBK) (41). The exposed 2'-hydroxyl groups of the last G residues of the G tracts that preceded the two loops (UUA segments) are indicated (arrows). **(B)** Gene-specific primer extension of an ectopically expressed G3U quadruplex probed with NAI in vitro (after folding in either 0 or 150 mM K⁺) or in HEK293 cells. Shown is a phosphorimage of a denaturing gel that resolved the extension products of a P³³-radiolabeled primer. RT stops corresponding to the preferential modifications of NAI within the G3U quadruplex are indicated (blue dots, G residues; green dots, U residues), which included the modifications specific to the folded quadruplex (blue dots). **(C)** RT-stop profiles of two RG4s and their flanking regions within the *Malat1* RNA, showing read counts color-coded according to the identity of the template nucleotide at the stall (position 0). G residues preferentially modified in the presence of 150mM K⁺ are indicated (blue arrowheads).

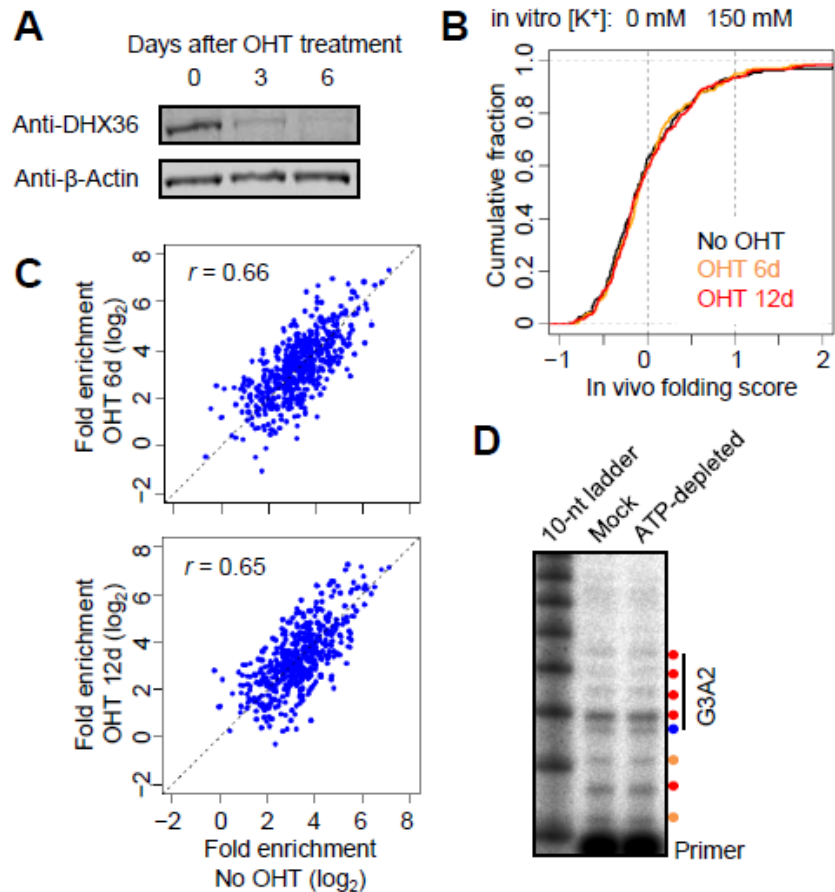


Fig. S8. Robust unfolding of RG4 regions in vivo, despite depletion of either DHX36 or ATP. **(A)** Decrease in DHX36 protein levels in MEFs after adding 1 μ M 4-hydroxytamoxifen (OHT), which induces Cre-mediated loss of the *Dhx36* gene. Shown is an immunoblot probed for DHX36 (*top*) and β -Actin (*bottom*), which served as the loading control. After 6 days of OHT treatment, DHX36 protein decreased >95%. **(B)** In vivo folding scores observed after deleting *Dhx36* (6 or 12 days after OHT treatment, OHT 6d and 12d, respectively) compared to those observed after no deletion (no OHT). Shown are distributions of scores for the 268 RG4 regions quantified in all three samples. **(C)** Correspondence between the RT-stop signals observed with and without *Dhx36* deletion. Scatter plots show the fold enrichment values for RT-stop signals of each RG4 region observed after 6 or 12 days of OHT treatment relative to those observed after no treatment (*top* and *bottom*, respectively). Spearman's correlation coefficients are shown (r). **(D)** DMS probing of the G3A2 quadruplex in yeast cells either after depleting ATP or after mock depletion. To deplete ATP, exponential-phase yeast were treated with 10 mM sodium azide and 10 mM deoxyglucose for 1 hour. Otherwise, as in Fig. 4D.

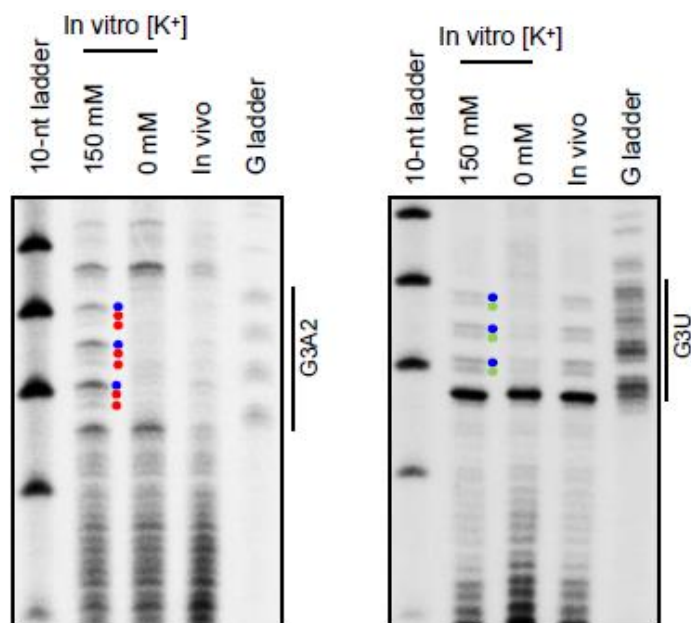


Fig. S9. NAI probing of the G3A2 (*left*) and G3U (*right*) quadruplexes in *E. coli*. Stops at modifications specific to the folded RG4 structures are indicated (blue, G residues; red, A residues; green, U residues). The G ladders were generated as in fig. S6E. The primer was end-labeled with P^{33} . As expected from the results of DMS probing (Fig. 6C), intracellular NAI probing of the G3U quadruplex yielded a strong signal for the pattern of modifications specific to the folded quadruplex. In contrast, intracellular NAI probing of the G3A2 quadruplex yielded only a weak signal for the pattern of modifications specific to the folded quadruplex. This apparent discrepancy with the results of DMS probing for the G3A2 quadruplex (Fig. 6B and C) might be due to either protein binding in vivo that occluded NAI modification at diagnostic 2'-hydroxyl groups, diminishing the signal in this assay, or protein binding in vivo that occluded DMS modification at diagnostic N7 positions of G residues, causing a false positive in the analyses of Fig. 6B and C.

Reference

39. Palenik B, et al., The genome of a motile marine *Synechococcus*. *Nature* **424**, 1037-1042 (2003). doi: 10.1038/nature01943; pmid: 12917641
40. K. S. Pollard, M. J. Hubisz, K. R. Rosenbloom, A. Siepel, Detection of nonneutral substitution rates on mammalian phylogenies. *Genome Res* **20**, 110-121 (2010). doi: 10.1101/gr.097857.109; pmid: 19858363
41. G. W. Collie, S. M. Haider, S. Neidle, G. N. Parkinson, Acryystallographic and modelling study of a human telomeric RNA (TERRA) quadruplex. *Nucleic Acids Res.* **38**, 5569–5580 (2010). doi: 10.1093/nar/gkq259; pmid: 20413582

Additional Data table S1 (separate file)

Strong RT stops of mESCs and identification of RG4 regions.

Additional Data table S2 (separate file)

RG4 regions in the HEK293T and HeLa transcriptomes.

Additional Data table S3 (separate file)

Quantification of in vitro and in vivo folding of RG4 regions in mESCs.

Additional Data table S4 (separate file)

Identification and DMS probing of RG4 regions in *S. cerevisiae*.

Additional Data table S5 (separate file)

Quantification of NAI modifications of RG4 regions in mESCs.

Additional Data table S6 (separate file)

DMS probing of RG4 regions in bacteria.